Energy Conversion and Management 333 (2025) 119794

Contents lists available at ScienceDirect

Energy Conversion and Management

journal homepage: www.elsevier.com/locate/enconman

Oscillating water column wave energy converter with flexible structured sheet material for enhanced power output

Yang Huang [a], Guillermo Idarraga [b], Farhad Abad [a], Qing Xiao [a,*], Liu Yang [b], Saishuai Dai [a], Saeid Lotfian [a], Feargal Brennan [a]

[a] Department of Naval Architecture, Ocean & Marine Engineering, University of Strathclyde, Glasgow, UK
[b] Advanced Composite Group, Department of Mechanical and Aerospace Engineering, University of Strathclyde, Glasgow, UK

ARTICLE INFO

Keywords:
Flexible wave energy converter
Structured sheet material
Membrane pre-stretching
Computational fluid dynamics, Fluid-structure interaction

ABSTRACT

Flexible wave energy converters (FlexWECs) are increasingly recognized for their potential to improve efficiency, reliability, and survivability in extreme ocean conditions. This study explores two strategies to enhance FlexWEC performance: customizing material properties and optimizing structural configuration. A structural sheet material with a specific pattern was developed to increase device power output under lower external loading, while membrane pre-stretching was investigated to tune the system's natural frequency and improve dynamic response. The material's mechanical behaviour was characterized through uniaxial tests, and a hyper-elastic YEOH model was applied to describe its nonlinear response. High-fidelity fluid–structure interaction simulations were performed to compare the performance of a flexible oscillating water column wave energy converter (WEC) using the newly developed structural sheet material against conventional natural rubber, with a focus on fluid dynamics, membrane deformation, stress distribution, and power output. The results indicate that, compared to natural rubber, the structural sheet material increases membrane deformation by 143%, reduces maximum stress by 14% at resonance, and boosts power output by 245%. Additionally, pre-stretching significantly increases the WEC system's natural frequency, promotes a more uniform stress distribution, which reduces fatigue risk, and increases power output by 54%. These findings highlight the potential of these strategies to enhance FlexWEC efficiency and reliability, offering valuable insights for adapting such systems to complex and variable marine environments.

1. Introduction

Conventional wave energy converter (WEC) designs typically utilize rigid body systems to interface with waves, transferring mechanical motion to a point-load power take-off (PTO) system [1]. This often involves mechanical turbomachinery driving an electromagnetic generator, similar to those used in wind and tidal energy systems [2]. However, the deployment of rigid-body systems with complex energy harvesting chains in marine environments faces significant challenges. High loads and corrosive conditions adversely affect metallic machinery, leading to premature fatigue failures. Consequently, these designs are large, heavy, and often overly robust to meet reliability standards, resulting in high costs and limited adaptability to varying wave climates [3,4].

To address the reliability and survivability challenges of conventional WEC designs, flexible wave energy converters (FlexWECs) using rubber-like elastomeric composite structures are gaining increasing attention [1,5–8]. FlexWECs offer several advantages over traditional WECs. The integration of flexible structures simplifies the overall system design, particularly through the incorporation of dielectric elastomer generators (DEGs) into the working surface [3,9]. This integration reduces the complexity of the PTO system and enhances system reliability. Moreover, DEGs shorten the energy harvesting chain by allowing direct conversion of wave energy into kinetic energy via the primary mover, bypassing the mechanical conversion required in traditional turbomachinery designs and thereby improving efficiency [10,11]. Additionally, flexible structures can withstand high loads in marine environments through passive deformation, and the use of rubber-like flexible materials improves corrosion resistance [3]. These features increase the adaptability and survivability of FlexWECs in harsh marine conditions.

Among the numerous WEC designs, the oscillating water column (OWC) is one of the most attractive and extensively studied [12–14].

* Corresponding author.
E-mail address: qing.xiao@strath.ac.uk (Q. Xiao).

https://doi.org/10.1016/j.enconman.2025.119794
Received 20 October 2024; Received in revised form 8 March 2025; Accepted 5 April 2025
Available online 10 April 2025
0196-8904/© 2025 The Authors. Published by Elsevier Ltd. This is an open access article under the CC BY license (http://creativecommons.org/licenses/by/4.0/).

This is primarily due to its simple structural design and minimalist layout. The OWC WEC system consists of a submerged hollow structure, open at the bottom to incoming waves and closed at the top by a circular diaphragm DEG. The device contains both a water column and an air column. As waves impact the semi-submerged structure, the resulting inflation and deflation of the DEG occur. By properly charging and discharging the DEG during its cyclical deformation, the OWC WEC converts ocean wave energy into electricity [4].

A number of experiments and numerical studies have been conducted to validate the concept of DEG-based OWC and investigate the performance of this novel FlexWEC design under various wave conditions. Rosati et al. [13] proposed a theoretical model for DEG-based PTO, establishing a reduced, dynamic model for inflated circular diaphragm DEG, which accounts for dielectric elastomer viscoelasticity. This computationally simple model can be easily integrated into wave-to-wire models of OWCs for fast analysis and real-time applications [15]. Subsequently, Vertechy et al. [12] introduced a promising concept of a DE-based WEC, the Polymeric Oscillating Water Column (Poly-OWC), and analysed the viability of using DE generators as PTO systems through a simplified hydraulic-electro-hyper-elastic model. Further research by Moretti et al. [16] and Gastone et al. [17] demonstrated that the DEG system could convert wave energy carried by the OWC into electricity in a wave-flume facility. A DEG-based PTO prototype, built using a commercial polyacrylate film, achieved a maximum power output of 0.87 W at resonant frequency. Building on this, Moretti et al. [18] proposed an improved architecture, known as the polymer-based axial-symmetric OWC (Poly-A-OWC), featuring an axial-symmetric U-shaped collector with a circular diaphragm DEG at its top. They developed a novel lumped-parameter nonlinear numerical model of the Poly-A-OWC to design and size its geometry. A small-scale prototype was built and tested in a wave tank facility to demonstrate the concept and validate the numerical models. Furthermore, Moretti et al. [19] conducted theoretical and experimental studies on a WEC combining the U-oscillating water column (U-OWC) and DEG PTO concepts. The lumped-parameter mathematical model was used for the theoretical study, and a small-scale prototype was preliminarily tested in a real-sea environment. The results demonstrated that the overall power output performance of this system is comparable to that of more conventional, costly, and complex PTO technologies. Moreover, Abda et al. [20] conducted dry tests to evaluate the material properties of various flexible materials and further investigated the fluid–structure interaction (FSI) behaviour of a flexible OWC WEC through 1:20 scale model experiments. The influence of flexible materials on the dynamic response of the system was explored.

To maximize wave energy capture, DEG-based OWC systems need to be designed such that their natural frequency closely matches the prevailing ocean wave frequencies. However, the variable nature of marine wave environments makes it challenging to meet this requirement. To overcome this limitation, Righi et al. [21] proposed a pressure differential WEC design consisting of a submerged air chamber with a horizontally mounted circular DEG at its top, which directly interacts with wave pressures. Experimental and numerical studies have shown that this design can achieve significant power output across a wide range of wave frequencies. Besides this, research aimed at enhancing the power output of DEG-based OWC WECs remains limited.

Building upon existing research, this study explores two strategies to enhance the power output of flexible OWC WECs. The first strategy involves adjusting the pre-stretching applied to the DEG membrane to optimize system stiffness. The second approach focuses on the development of advanced materials for the DEG membrane to improve its structural response. These two strategies aim to enhance the overall performance of flexible WECs from both structural and material perspectives.

Structurally, the system's natural frequency can be dynamically adjusted by varying the pre-stretching applied to the DEG membrane, aligning it with the frequency of incoming waves to achieve near-resonant responses and thus higher power output. While the primary function of pre-stretching is to enhance the stability of the DEG membrane and reduce hysteresis, it also significantly affects system stiffness and, consequently, the resonance frequency.

From a materials perspective, developing a new material for the DEG membrane that deforms more under smaller pressures and less under higher pressures could enhance power output while preventing excessive deformation-induced failure. This seemingly contradictory requirement is feasible with structured sheet materials. Structured sheet materials, consisting of an isohedral pattern of elastic rods, offer a tailored mechanical response governed by the pattern's configuration. As the sheet deforms, its stiffness increases in accordance with the alignment of the rods to the applied force, enhancing deformability and stress distribution [22]. By customizing structured sheet materials to meet the deformation demands of FlexWECs, converter performance can be significantly optimized [23–25].

To validate the proposed strategy, this study examines the impact of pre-stretching the DEG membrane and using structural sheet materials on the FSI responses and power output of flexible OWC WECs. A structured sheet material made from natural rubber is developed and characterized through uniaxial tests, with the material properties subsequently used in the FSI simulation of a flexible OWC WEC. To obtain accurate results and detailed information on the flow field and structural dynamics, we utilize a computational fluid dynamics (CFD)-finite element analysis (FEA) analysis tool developed in our previous work for FlexWECs [26]. The OWC WEC with structured sheet materials is simulated under regular waves, considering a small pre-stretching of 10 % on the flexible membrane to fine-tune the system's stiffness. The results evaluate the membrane deformation, stress distribution, flow field, and power output, providing insights into the potential performance enhancements offered by structured sheet materials and pre-stretching in FlexWECs.

This paper is structured as follows: Section 2 introduces the developed structured sheet material and the material characterization tests. Section 3 describes the numerical simulation methods and computational settings. Section 4 presents the FSI responses of the flexible OWC WEC with structured sheet material and pre-stretching, investigating the impact from the perspectives of flow field, structural response, and power output. Finally, the conclusions are summarized.

2. Structural sheet material

To enhance the power output of the FlexWEC while preventing structural failure due to excessive membrane deformation, a structured sheet material was developed using natural rubber (NR) with a specific pattern 937 designated as NR937. This material underwent uniaxial tests to determine its stress–strain curve. Subsequently, a hyper-elastic model was fitted to accurately capture its nonlinear properties for use in further numerical simulations.

2.1. Material characterization

As shown in Fig. 1(a), the structured sheet material NR937 features a planar network of interconnected elastic rods with a rectangular cross-section. This design is selected for its zigzag arrangement, which functions like springs. When stretched, the unfolding of these "springs" generates a significantly stiffer elastic response. At this point, the material aligns with the load path, substantially increasing its stiffness. This behaviour indicates that the structured sheet exhibits anisotropic and nonlinear in-plane stiffness.

The natural rubber used to create the structured sheet material was provided by Coruba UK [27]. According to the datasheet, it has a thickness of 3 mm, a hardness of 38° Shore A, a strength of 23.5 MPa, a failure strain of 810 %, a density of 980 kg/m3, and a Poisson's ratio of 0.5. The structured sheet material sample made from this rubber is shown in Fig. 1(b).

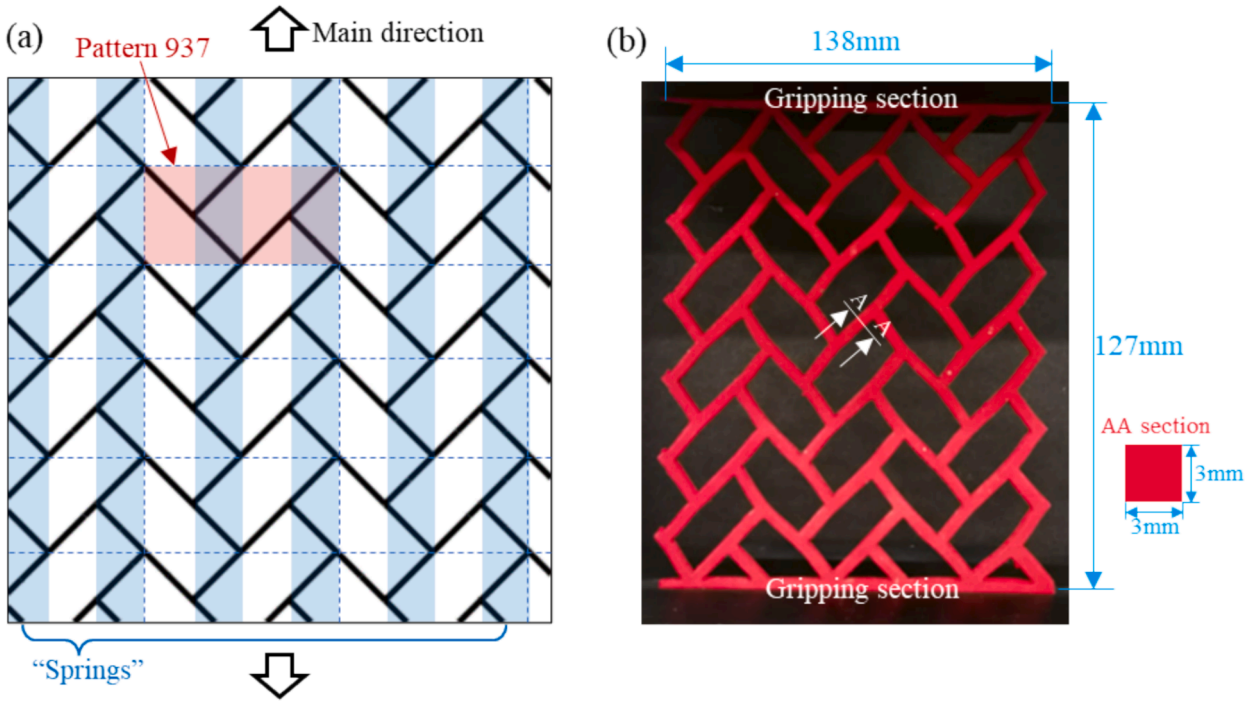

Fig. 1. (a) Structural pattern 937; (b) Structural sheet material NR937 sample.

The mechanical behaviour of NR and NR937 was characterized under uniaxial conditions using a computer-controlled Testometric 500X-50 universal servo-electric test machine, equipped with a calibrated 50 kN load cell [28,29]. Each elastomer was evaluated with at least five samples.

2.2. Hyper-elastic model

The experimental results for the uniaxial tests of NR and NR937 are presented in Fig. 2. Overall, NR937 exhibits lower stiffness compared to NR, particularly at lower strain levels (10 % $< \varepsilon <$ 40 %), which is the strain range primarily encountered in the current numerical simulations. In this range, the "stiffness" ($\Delta\sigma/\Delta\varepsilon$) of NR937 is approximately 9 % to 64 % of that of NR. As the strain increases, the difference in stiffness between the two materials decreases. This indicates that under lower external forces, NR937 deforms more than NR due to its lower stiffness, thereby enhancing the power output of the FlexWEC.

Additionally, the stress–strain curves for both materials display evident nonlinear behaviour. To accurately describe these nonlinear properties, the YEOH hyper-elastic model based on a strain energy potential is adopted [30].

$$E = \sum_{i=1}^{N} C_{i0}(\overline{I_1} - 3)^i + \sum_{i=1}^{N} \frac{1}{D_i}(J-3)^{2i} \quad (1)$$

where I_1 signifies the modified first invariant of the Cauchy-Green deformation tensor, while C_i and D_i are material constants ascertained through experimental results. The hyper-elastic constants are derived by fitting the stress–strain curves obtained from the experimental data using Abaqus, assuming material incompressibility and employing a third-order strain energy potential. The fitted results, which align well with the experimental data, are shown in Fig. 2. The parameters for the YEOH model used to describe the material properties are listed in Table 1.

It is important to highlight that, unlike NR, NR937 is an anisotropic

Table 1
Hyper-elastic constants of YEOH model for NR and NR937.

Materials	C_{10}(MPa)	C_{20}(MPa)	C_{30}(MPa)
NR	2.40E-01	−4.14E-03	1.83E-04
NR937	3.63E-02	2.50E-02	−1.64E-03

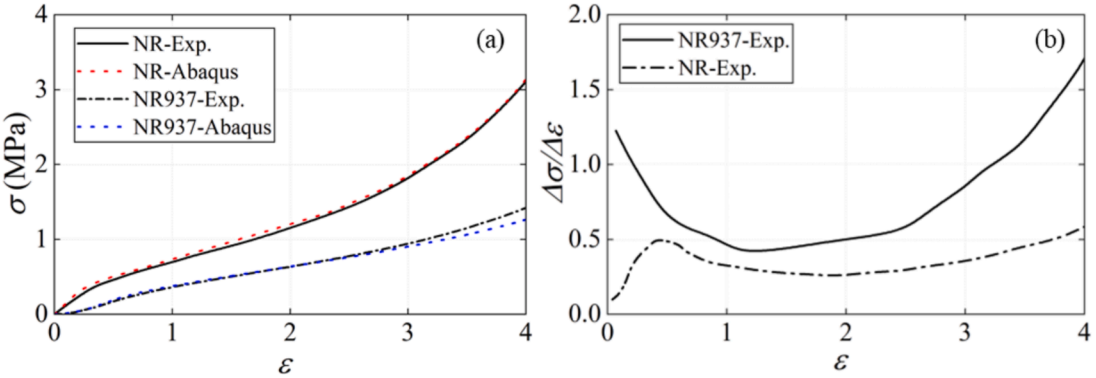

Fig. 2. Strain-stress curves of natural rubber (NR) and structured sheet material (NR937).

material. The uniaxial tests conducted only characterize its properties in the primary loading direction, which does not fully capture its behaviour under symmetrical loading conditions. However, in practical applications, the membrane at the top of the OWC WEC is subjected to symmetrical loads. As a result, NR937 cannot be directly applied to the flexible membrane of an OWC WEC.

To address this, we assume the existence of a structural sheet material that satisfies the following criteria: (a) It is an isotropic, homogeneous, solid flexible material. (b) Its stress–strain behaviour matches the experimentally measured stress–strain response of NR937 in its primary loading direction.

Theoretically, such a structural sheet material can be realized by appropriately modifying the structural pattern. For convenience, we continue to refer to this new isotropic structural sheet material as NR937 throughout this study, which is the flexible material employed in our numerical simulations.

Additionally, the structural sheet material features a perforated design, requiring a thin solid layer to cover both its upper and lower surfaces when applied to the OWC WEC. To simplify the calculations, only the stiffness of the structural sheet material is considered. Therefore, in the subsequent numerical simulations, we model it as an isotropic, homogeneous, solid flexible material, assuming its hyperelastic properties to be equivalent to those of NR937.

3. Numerical set up

3.1. FSI analysis tool

In our previous work, we developed a coupled FSI analysis tool that integrates CFD and FEA for simulating complex FSI problems [26,31–33]. To verify the reliability and accuracy of this tool, we conducted simulations on various benchmark cases, including a 3D flexible plate in uniform water current, the deformation of a floating elastic disk in regular ocean waves, and the FSI responses of both flexible OWC WECs and flexible tube WECs. The results demonstrated good agreement with experimental data and other numerical studies [26]. Given this extensive prior validation, we have not repeated the validation process in this work. Instead, this tool is directly employed to simulate the FSI responses of flexible OWC WECs incorporating structured sheet materials. A brief overview of the FSI tool is provided in this sub-section.

3.1.1. Governing equations

The transient viscous flow around the WEC is governed by the three-dimensional incompressible Navier-Stokes equations:

$$\nabla\cdot\boldsymbol{U}=0 \tag{2}$$

$$\frac{\partial(\rho\boldsymbol{U})}{\partial t}+\nabla\cdot\left(\rho\left(\boldsymbol{U}-\boldsymbol{U}_{\mathrm{g}}\right)\right)\boldsymbol{U}=-\nabla p_d-\boldsymbol{g}\cdot\boldsymbol{x}\nabla\rho+\nabla\cdot(\mu\nabla\boldsymbol{U})+(\nabla\boldsymbol{U})\cdot\nabla\mu+\boldsymbol{f}_{\sigma} \tag{3}$$

where $\boldsymbol{U}$ represents the flow velocity, $\boldsymbol{U}_{\mathrm{g}}$ denotes the mesh grid velocity, ρ stands for the mixed density of the air and water phases, p_d signifies the dynamic pressure, $\boldsymbol{g}$ is the gravitational acceleration vector, μ indicates the dynamic viscosity, and $\boldsymbol{f}_{\sigma}$ refers to the surface tension term.

The finite volume method (FVM) is employed to discretize the governing equations in the fluid domain, while the volume of fluid (VOF) method [34] is used to capture the free surface dynamics. Pressure-velocity coupling is handled using the PIMPLE algorithm [35], which iteratively solves the nonlinear equation system. For temporal discretization, the second-order Crank-Nicolson scheme is applied, ensuring accuracy in time-dependent computations. The convective terms are discretized using a second-order upwind scheme, while the gradient terms are approximated using a second-order cell-limited Gauss linear scheme to enhance numerical stability and accuracy.

Additionally, considering the wave frequencies of 0.3 ~ 0.9 Hz and the small wave amplitude of 0.05 m in this study, we estimated the Reynolds number across the computational domain, with results remaining below 1×10^4. Furthermore, analysis of the flow field shows no significant free surface breaking, no large-scale flow separation, and no vortex shedding induced by fluid–structure interaction. Therefore, using a laminar model is acceptable for this study.

The governing equations for structural dynamics are the weak form of the momentum balance equations, expressed as:

$$\rho_s\frac{D^2\mathbf{U_s}}{D^2t^2}=\nabla\cdot\mathbf{P}+\rho_s\mathbf{f} \tag{4}$$

$$\mathbf{P}=\mathbf{C}:\mathbf{E},\quad \mathbf{E}=\frac{1}{2}\left(\mathbf{F}^{\mathbf{T}}\mathbf{F}-\delta\right) \tag{5}$$

where ρ_s denotes the material density, and $\mathbf{U_s}$ is the displacement vector. The term $\mathbf{P}$ represents the second Piola-Kirchhoff stress tensor, while $\mathbf{f}$ indicates the body forces. The material's elasticity is characterized by the tensor $\mathbf{C}$, and $\mathbf{E}$ denotes the Green-Lagrange strain tensor. Furthermore, $\mathbf{F}$ is the deformation gradient, and δ is the identity tensor.

The finite element method (FEM) is employed to discretize the governing equations in the solid domain. The Newmark-β method is used for implicit time integration, incorporating geometric nonlinearity to accurately capture the structural response.

3.1.2. Coupling strategy

The FSI analysis tool employed in this study integrates OpenFOAM [36] for fluid dynamics, CalculiX [37] for structural response analysis, and preCICE [38] for coupling the fluid and solid components. A partitioned coupling scheme is adopted due to the use of different numerical methods for the fluid and solid domains. As illustrated in Fig. 3, the fluid and structural solvers independently compute the flow field and structural deformation while exchanging data at the fluid–structure interface.

To enhance numerical stability, a strong coupling strategy is implemented. Additionally, an implicit scheme is utilized, allowing for larger time steps while maintaining numerical stability and reducing computational costs. Furthermore, an improved IQN-ILS method [39] is incorporated to stabilize and accelerate the coupling iterations.

Given the differences in the fluid and solid meshes, data exchange between the two domains is facilitated through data mapping and interpolation at the fluid-solid's interface. For data transfer, an interpolation method based on radial basis functions (RBF) is employed to transfer nodal forces from the fluid to the solid domain, while vertex displacements are transferred in the opposite direction [40]. Two distinct mapping schemes, conservative and consistent, are implemented within the RBF interpolation. To ensure energy balance at the interface, the conservative scheme, which ensures that the sum of the data values on both sides remains equal, is applied for force mapping, while the consistent scheme is adopted for displacement mapping.

To assess the convergence of the FSI coupling towards a monolithic solution, the discrete l_2-norm of the difference between solutions from consecutive iterations is computed. The simulation advances to the next time step once the l_2-norm satisfies the prescribed convergence criterion or when the maximum iteration limit is reached.

3.2. Geometry model

The Poly-A-OWC model proposed by Moretti et al. [18] is selected for the numerical simulations. As shown in Fig. 4(a), this model features an axis-symmetric U-shaped collector and a circular diaphragm dielectric elastomer generator (CD-DEG) as the PTO. In our CFD simulations, the CD-DEG PTO is modelled as a flexible membrane. It is noted that the electric field applied to the PTO can reduce the material stiffness and increase the system's damping. However, limited by the capability of the FSI tool, the influence of the electric field is ignored in the simulation. The flexible membrane has a diameter of 0.4 m and an initial thickness of 2 mm. The main geometric parameters are presented in Fig. 4(a), with

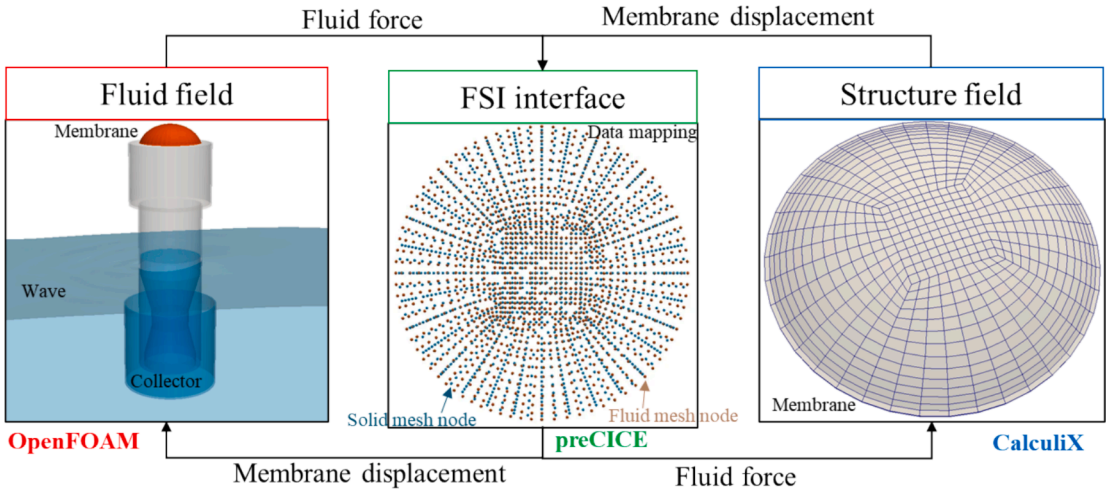

Fig. 3. Coupling strategy of the FSI simulation for the flexible OWC WEC.

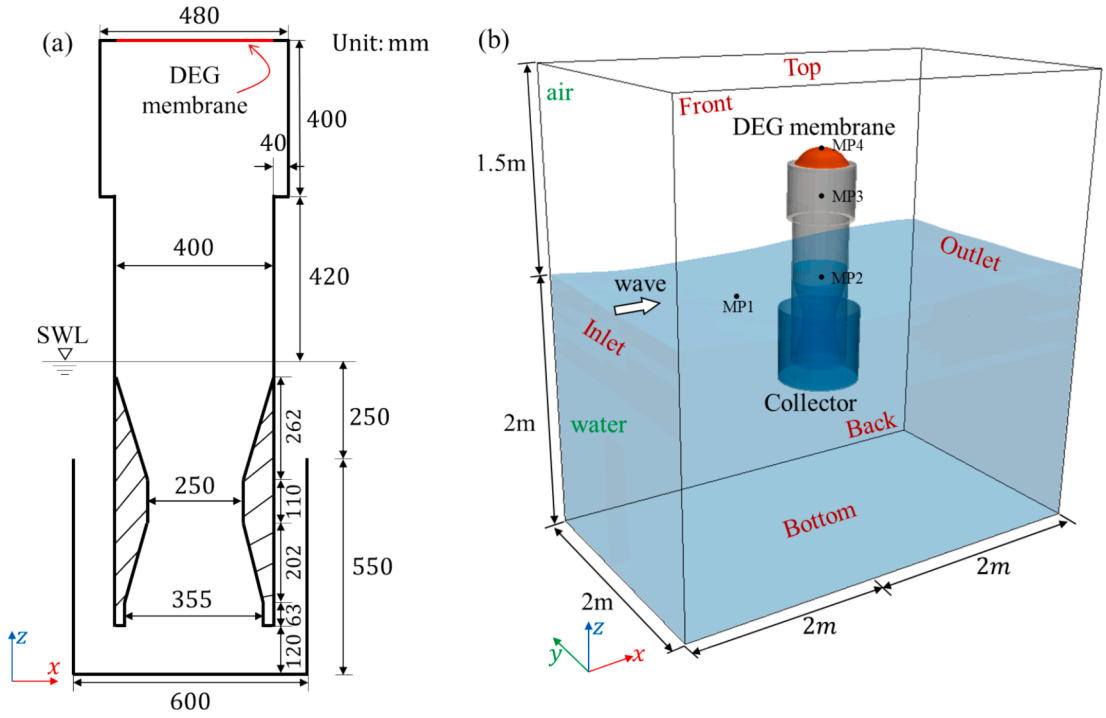

Fig. 4. (a) Longitudinal section of the Poly-A-OWC model; (b) Computational domain.

more detailed information available in the literature [18].

3.3. Computational parameters

As shown in Fig. 4(b), the model is fixed at the centre of the cubic computational domain, 2 m from both the inlet and outlet boundaries, and 1 m from the front and back boundaries. The water depth in the computational domain is 2 m. Notably, the active wave absorption technique is adopted [41,42], which prevents wave reflection and significantly reduces the length of the computational domain, thereby decreasing the total number of required grids. Additionally, four monitoring points (MP1 ~ MP4) are designated to track the incident wave, water elevation in the collector, air chamber pressure, and membrane tip displacement.

To accurately capture the fluid–structure interaction response of the flexible membrane, the grid around the flexible membrane and the free surface is refined, with minimum cell sizes of 2.5×10^{-3} m and 5×10^{-3} m, respectively. The computational domain contains 1.21 million grid cells, with the grid distribution shown in Fig. 5. For the structural analysis, as shown in Fig. 6(a), the membrane's edges are fixed, and it undergoes periodic deformation under internal and external pressure differences. The flexible membrane is modelled using 660 twenty-node brick elements (C3D20) [43], as depicted in Fig. 6(b). To improve the stability of the FSI simulation, Rayleigh damping with $\alpha = 0.02$ and $\beta = 0.05$ is applied.

In this study, regular waves with various frequencies are considered using Stokes' second-order wave theory to generate incident waves. Additionally, scenarios with and without a 10 % pre-stretching of the structured sheet material are investigated to understand the influence of pre-stretching λ_p, which is defined by the following equation:

$$\lambda_p = (d_p - d_0)/d_0 \tag{6}$$

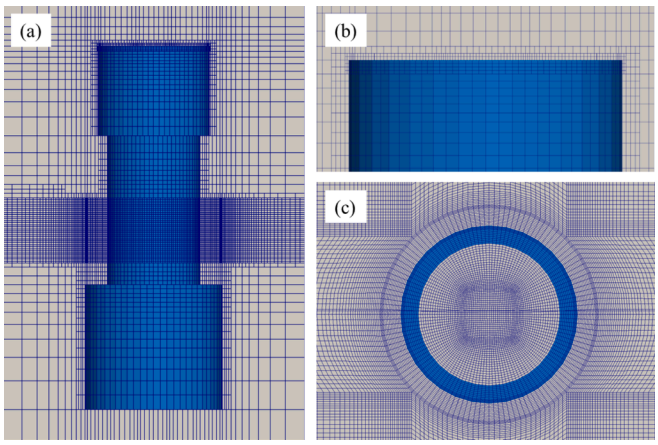

Fig. 5. Grid distribution near the OWC model: (a) overview; (b) near membrane; (c) near free surface.

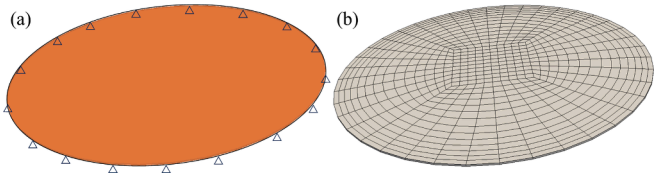

Fig. 6. (a) Schematic diagram of a flexible membrane; (b) Structural mesh.

Where d_0 is the initial diameter of the flexible membrane, and d_p is the diameter after pre-stretching. The specific simulation conditions are summarized in Table 2. Notably, in cases where pre-stretching is applied, the thickness and diameter of the stretched flexible membrane are 2 mm and 0.4 m, respectively, consistent with the membrane dimensions in cases without pre-stretching.

The boundary conditions for the computational domain are defined as follows: At the inlet, the velocity is specified according to the incident wave parameters. A zero-gradient condition is applied at the outlet boundary, while the top boundary is set as a pressure outlet, and a no-slip condition is enforced at the bottom boundary. Furthermore, symmetry conditions are imposed on the front and back boundaries.

4. Results and discussions

This section presents the simulation results of the flexible OWC WEC with natural rubber and structured sheet material under various wave frequencies. Subsection 4.1 focuses on the FSI responses of the WEC, including flow field, structural dynamics, and power estimation. Subsection 4.2 compares the FSI responses and power output of the WEC with structured sheet material and natural rubber. Subsection 4.3 investigates the influence of pre-stretching on the WEC's FSI responses and power output.

4.1. Grid and time step convergence test

To ensure the accuracy and stability of numerical simulations, grid and time step convergence tests are conducted. Three sets of grids with different mesh resolutions, named coarse, medium, and fine, are used. The minimum grid sizes are $1.25 \times 10^{-2}D$, $6.25 \times 10^{-3}D$, and $3.125 \times 10^{-3}D$ (D is membrane diameter), respectively, with total grid numbers of 0.85 million, 1.21 million, and 1.86 million. Additionally, three different time step sizes $\Delta t = 1 \times 10^{-3}$ s, 2×10^{-3} s, and 4×10^{-3} s are evaluated for time step sensitivity using the medium mesh. The medium time step size is approximately 1.6×10^{-3} times of the smallest wave period. Regular waves with a period of 2.0 s and amplitude of 0.05 m were selected for these tests. The Poly-A-OWC WEC with structured sheet material NR937 was simulated using these different mesh resolutions and time step sizes, and the results are shown in Fig. 7. The predicted deformation of the membrane centre point showed small discrepancies between the medium and fine meshes, and the discrepancies among the three time-step sizes are also small. Considering the enhanced stability of the present FSI analysis tool with smaller time steps, the smallest time step of 1×10^{-3} s and the medium mesh were chosen for the subsequent numerical simulations.

Additionally, to verify that the wave tank adopted in this work is sufficiently large to generate the desired regular waves, we analysed the temporal variation of wave elevation at different locations, e.g. x = -1.5 m, −1.0 m, −0.5 m, 0 m, 0.5 m, 1.0 m, 1.5 m, along the wave propagation direction. The results, shown in Fig. 8, demonstrate that both the wave period and height closely match the prescribed values, indicating that the current domain size is adequate for generating the required waves.

Table 2
Summary of simulation conditions.

Lode case	Wave frequency f_w(Hz)	Wave amplitude A_w(m)	Material	Pre-stretching λ_p
LC1	0.30 ~ 0.70	0.05	NR937	0
LC2	0.40 ~ 0.80	0.05	NR	0
LC3	0.40 ~ 0.90	0.05	NR937	10 %

4.2. FSI responses of flexible OWC WEC

To better understand the mechanism and complex FSI response of the flexible WEC, we analyse a case in which the WEC reaches its resonance. Under this condition, the membrane deformation reaches its maximal, occurring at a specific wave period of 1.82 s. The wave height is 0.05 m, and the membrane is composed of structured sheet material NR937, with no pre-stretching applied.

4.2.1. Fluid field

As shown in Fig. 9, the interaction between the flexible membrane and waves at different time points within one wave cycle is presented. The free surface and air chamber are coloured based on wave elevation and dimensionless pressure $(p - p_a)/(\rho g A_w)$, where p_a is atmospheric pressure, ρ is the density of water. It can be observed that as the incident wave passes through the collector, pressure variations caused by changes in wave height drive the oscillation of the water column inside the collector. This oscillation compresses and stretches the "air spring", leading to periodic pressure fluctuations in the air chamber that cause the flexible membrane to deform upward and downward due to the internal and external pressure differences.

Additionally, the instantaneous pressure distribution in the air chamber is uniform, so a point located 0.5D (D is membrane diameter) below the centre of the membrane in the air chamber is selected as the monitoring point for time-history analysis, as shown in Fig. 10(c). The maximum pressure fluctuation amplitude in the air chamber is approximately 1714 Pa. Using the ideal gas law, we can estimate the air volume changes in the air chamber following pressure variations, based on the formula provided in [4].

$$v = v_0 \left(\frac{p_a}{p_a + p} \right)^{1/\gamma} \tag{7}$$

where, v and v_0 represent the air volumes inside the air chamber when the pressure difference between the air chamber and the external environment is p and 0, respectively. The specific heat ratio for air is γ = 1.4. Based on the numerical simulation, the maximum pressure fluctuation in the air chamber leads to a volume change of approximately 1.2 %, which is negligible. Therefore, the air is considered incompressible in

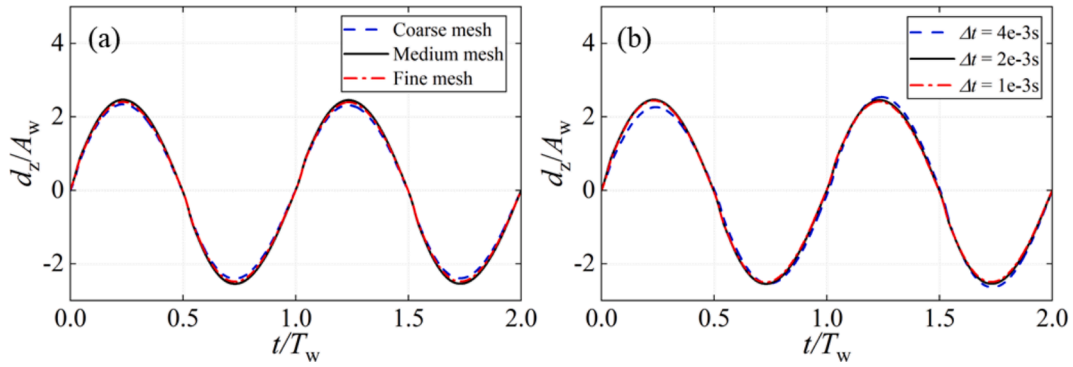

Fig. 7. Time history of deformation at the centre of membrane: (a) grid convergence test; (b) time step convergence test.

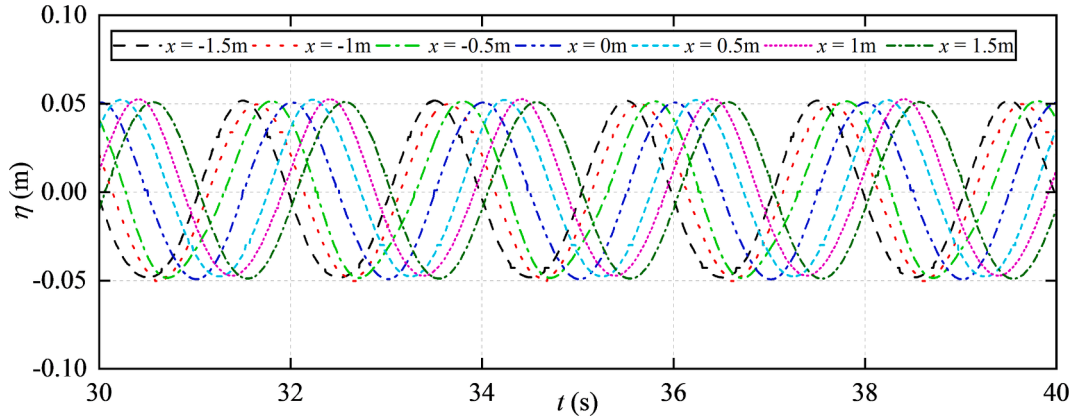

Fig. 8. Time history of wave elevation at different positions in the computational domain.

this study.

Furthermore, Fig. 10 presents the time-history curves of membrane tip displacement (d_z), water elevation inside the collector (η), and wave elevation 1 m in front of the OWC WEC (η_0). All these variables exhibit sinusoidal periodic variations. It can be observed that the wave elevation outside the collector is 90 degrees out of phase with the water elevation inside the collector, indicating that the incident wave drives the OWC's oscillation. Additionally, the phase of the OWC's motion, the air chamber pressure, and the membrane tip displacement are nearly identical. For traditional mechanical PTO systems, this implies that the work done by the air chamber pressure on the flexible membrane is entirely dissipated, rather than converted into electrical energy. However, for DEG-based PTO systems, this is expected, as energy conversion occurs through capacitance changes caused by membrane deformation, independent of pressure phase. A detailed analysis of energy extraction in the OWC WEC will be provided in subsequent sections.

To gain a deeper understanding of the flow dynamics within the OWC WEC, we visualize the velocity and vorticity distributions inside the air chamber at different moments over one wave period, as shown in Figs. 9 and 10. Due to the diameter difference between the collector and the air chamber, a step forms at the transition, causing significant velocity variations as the air flows through. An interesting phenomenon occurs during the upward deformation of the membrane from its lowest position. The fluid velocity in the central region of the air chamber moves downward, while the velocity near the cylinder wall moves upward, as indicated in Fig. 11 (t = 0 T_w, 0.125 T_w, 0.75 T_w, 0.875 T_w). This is primarily caused by the greater deformation at the membrane's centre compared to its edges. Consequently, a distinct vortex structure forms within the air chamber. As illustrated in Fig. 12, these vortex structures rise along the cylinder wall, highlighted by red dashed circles. Such complex flow phenomena are not captured by reduced-order models based on potential flow theory, offering deeper insight into the intricate flow field dynamics within the air chamber.

4.2.2. *Structure dynamics*

Fig. 13 visually presents the deformation of the flexible membrane at different instants during a wave cycle. Overall, the deformation exhibits radial symmetry about the centre, with identical deformation at points equidistant from the centre, fixed edges, and maximum deformation at the centre. The membrane primarily deforms in the first mode, but near the equilibrium position, it displays characteristics of the second mode, as seen in Fig. 13 at t = 0 T_w and t = 0.5 T_w. Additionally, the membrane cross-sectional deformation in Fig. 15 further highlights this behaviour. When the deformation is small, the system behaves nearly linearly, allowing higher-order modes, such as the second mode, to emerge. As the deformation increases, nonlinearity becomes more prominent, and the lower-order modes, such as the first mode, dominate the system's response.

Furthermore, Fig. 14 illustrates the stress distribution on the membrane surface. As the membrane deformation increases, the corresponding stress gradually rises. Radially, from the centre to the edge, the stress first decreases and then increases, with the maximum stress occurring at the edge, followed by the central region. However, for the second-mode deformation observed at t = 0 T_w, the stress distribution differs, showing an initial increase from the center to the edge, followed by a decrease, and then a subsequent increase near the edge.

For DEG-based PTO systems, the membrane's thickness variation is directly related to the power output. Here, we selected two instances with larger and smaller membrane deformations to plot the cross-sectional deformation and stress distribution, as shown in Fig. 15. As the membrane deformation increases, its thickness decreases. Notably, compared to the case with smaller deformation (t = 0 T_w), the thickness

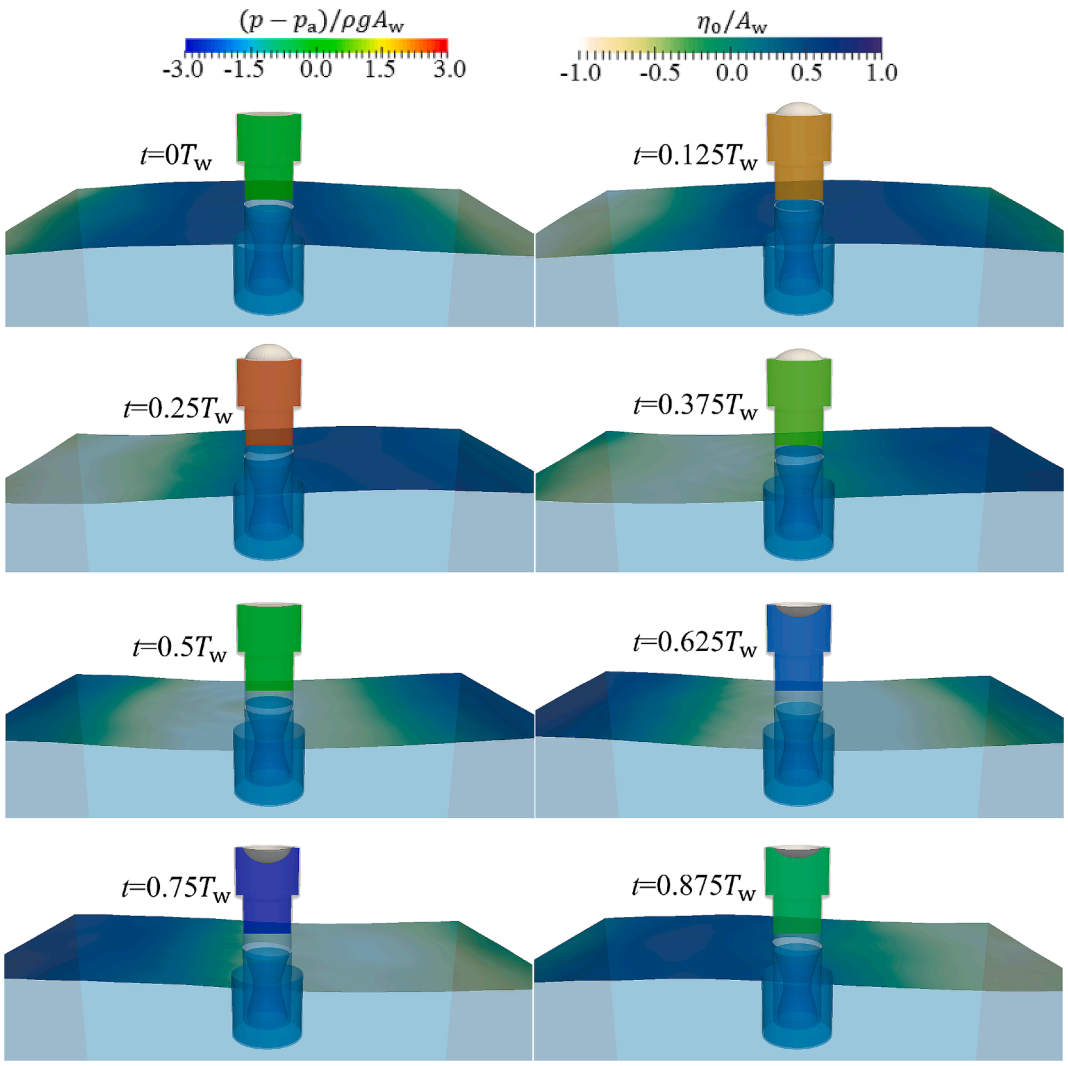

Fig. 9. Wave-flexible membrane interaction at different instants within one wave period (LC1: f_w = 0.55 Hz).

non-uniformity is more pronounced during larger deformation ($t = 0.75\ T_w$). In particular, the membrane's thickness is reduced in the centre and edge regions, as highlighted by the red dashed lines in Fig. 15(a), indicating stronger tensile forces and corresponding higher stresses, consistent with the results shown in Fig. 15(b). This thickness non-uniformity during deformation affects the charge distribution and power output. However, in the reduced-order model proposed by Vertechy et al. [44], the membrane's thickness is assumed to be uniform. In contrast, the current FEA simulation more accurately captures the detailed deformation behaviour of the membrane.

4.2.3. Power estimation

Unlike traditional mechanical PTO systems, which rely on fluid forces to drive a turbine or other mechanical devices to generate electricity, the flexible OWC WEC employs a DEG membrane for energy conversion. As shown in Fig. 16(a), the membrane undergoes thickness variation during deformation. By covering the membrane with electrodes and applying an electric charge, the DEG membrane acts as a variable capacitor. With an appropriate control circuit, the elastic potential energy released during the membrane's contraction can be converted into electrical energy. Fig. 16(b) illustrates the voltage-charge curve during different deformation stages of the membrane. OA represents the charging phase, where the membrane reaches maximum deformation. AB corresponds to the energy output as the membrane returns to its flat state, while BO indicates the discharge of the membrane by the control circuit. The shaded area, W_u, corresponds to the energy output per cycle. Detailed information on the DEG membrane's energy generation process and control methods can be found in references [15,17,18].

In the current FSI simulations, the PTO system is not considered, and the influence of the electric field on the structural response of the DEG membrane is also neglected. However, we can estimate the power output of the flexible OWC WEC based on the time-history curves of the membrane deformation. To calculate the energy output per cycle from the DEG membrane, we use the reduced model proposed by Rosati et al. [13].

$$W_u = \int_{\lambda_{max}}^{\lambda_{min}} \left[V\frac{dQ}{d\lambda} - \frac{d}{d\lambda}\left(\frac{1}{2}CV^2\right)\right] d\lambda \tag{8}$$

Where, Q and V represent the charge and voltage applied to the membrane, respectively, while C denotes the capacitance of the DEG membrane. These variables can be expressed as functions of the prevalent equi-biaxial stretch λ at the membrane's centre.

$$\lambda = \frac{h^2 + e^2}{ee_0} \tag{9}$$

$$C = \frac{nl^2\pi\varepsilon e e_0}{3t_0}\lambda\left(\lambda^2 + \frac{e}{e_0}\lambda + \frac{e^2}{{e_0}^2}\right) \tag{10}$$

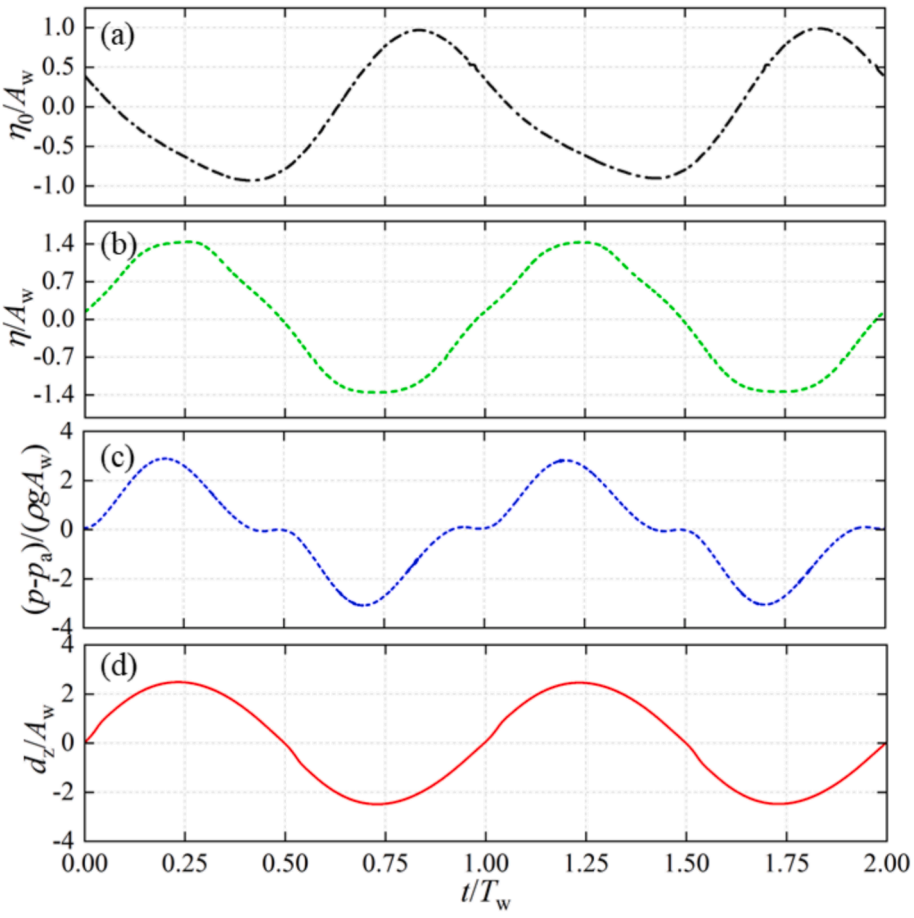

Fig. 10. Time history of different variables (LC1: $f_w = 0.55$ Hz): (a) wave elevation η_0 at watch point; (b) free surface η in OWC collector; (c) air-chamber pressure p; (d) tip displacement d_z of membrane.

$$V = E_{max} t_0 \lambda^{-2} \tag{11}$$

Where, e_0 represents the initial radius, e denotes the radius after pre-stretching, h is the vertical displacement at the center, t_0 is the initial thickness, nl represents the number of DEG layers, ε is the dielectric constant of the membrane, and E_{max} is the maximum electric field strength the membrane can withstand.

For the current flexible OWC WEC, assuming the use of DE acrylic elastomer VHB-4910 as the reference material, with $\varepsilon = 3.9825 \times 10^{-11}$F/m and $E_{max} = 65$ MV/m [17], and considering a single DEG layer, the maximum time-averaged power, based on the membrane deformation obtained from the FSI simulations, is 12.4 W. At a 1:20 scale, using Froude's scaling law, the projected full-scale power output of the device is estimated to reach 445 kW, highlighting its considerable potential for energy generation.

4.3. Impact of structured sheet material

Compared to NR, the structural sheet material NR937 has lower stiffness at low strain, as shown in Fig. 2. This allows the DEG membrane to undergo greater deformation under lower pressure, enhancing the power output of the WEC system. To better understand the impact of the structured sheet material on WEC performance, we conducted a comparative analysis of the flow field, structural response, and power output of WECs with NR937 and NR under different wave frequencies.

4.3.1. Air-chamber pressure and OWC amplitude

Fig. 17 presents the RAO of the OWC and the pressure variation amplitude within the air chamber at different wave frequencies for flexible OWC WECs using NR and NR937 materials. The RAO of the OWC is defined as A_η/A_w, where A_η is the amplitude of the OWC. When the membrane uses NR, both the RAO and air chamber pressure increase with wave frequency, peaking at $f_w = 0.55$ Hz, indicating the resonant frequency of the WEC system. A similar trend is observed with NR937, with the peak frequency also around 0.55 Hz. Although NR937 has much lower stiffness compared to NR, the material stiffness remains significantly smaller than the hydrodynamic stiffness of the WEC system, resulting in minimal impact on the system's resonant frequency. Furthermore, a comparison of the fluid dynamics at the resonant frequency shows that the pressure amplitude in the air chamber with NR937 is only 41 % higher than with NR, while the RAO with NR937 is 143 % greater than with NR.

We further compare the detailed flow fields, including velocity and vorticity, within the air chamber at different time instants at the resonant frequency for OWC WECs using different materials. Fig. 18 shows the results for NR, while the flow field response for NR937 is already presented in Figs. 9 and 10. Compared to NR, the use of NR937 results in larger OWC amplitudes, leading to higher fluid velocities in the air chamber, more distinct vortex structures, and more pronounced flow field variations.

4.3.2. Membrane deformation and stress distribution

The material significantly impacts the structural response of the flexible membrane. As shown in Fig. 19, we plot the deformation amplitude at the membrane centre and the maximum stress in the membrane under different wave frequencies. The deformation amplitude and maximum stress exhibit a similar pattern to the OWC's RAO, increasing with wave frequency, reaching a peak, and then decreasing.

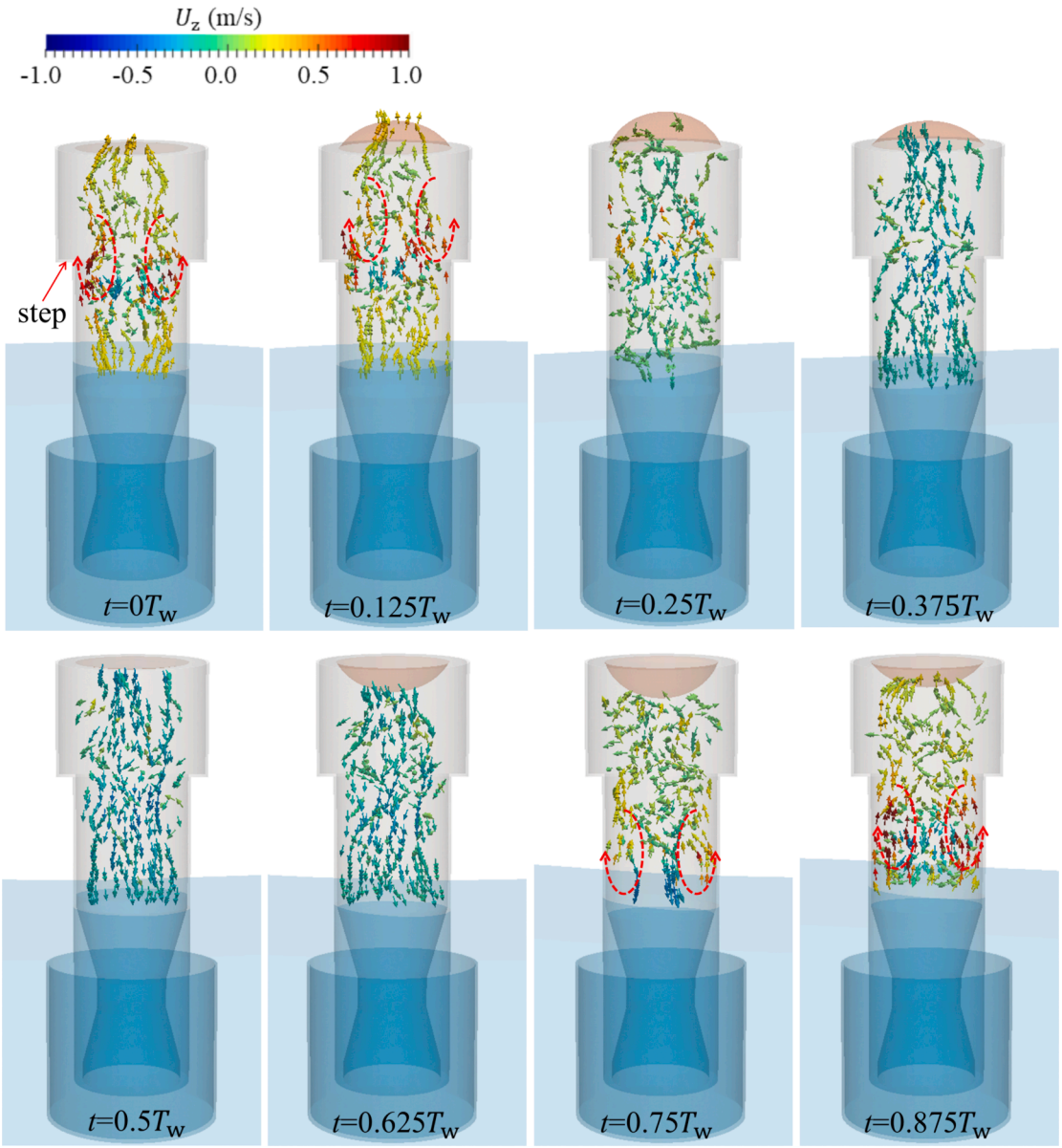

Fig. 11. Velocity distribution in the air chamber at various instants within one wave period (LC1, f_w = 0.55 Hz).

The peak frequencies for both NR and NR937 occur at 0.55 Hz.

In terms of magnitude, there are notable differences between NR and NR937. In the frequency range 0.3 Hz < f_w < 0.6 Hz, the deformation amplitude of the membrane with NR937 is 1.94 to 2.36 times greater than with NR, while the maximum stress is only 36 % to 86 % of that with NR. This demonstrates the advantage of using structural sheet material, which significantly increases deformation while maintaining lower internal stress. This enhances the WEC system's power output and reduces the risk of structural failure, improving overall system reliability.

Unlike simply using a more flexible material, structural sheet material offers further benefits. It allows the customization of material properties by adjusting the pattern, making it easier to achieve the desired characteristics. Additionally, the perforated design of the structural sheet material reduces weight and lowers material costs, which is crucial for scaling up flexible WEC systems.

We further plot the maximum deformation and stress distribution contours of the flexible membrane with different materials, as shown in Figs. 20 and 21. In terms of deformation shape, whether using NR or NR937, the circular membrane forms a nearly spherical cap, which aligns with the experimental observations [18,19].

For stress distribution, the maximum stress occurs at the membrane edges for both NR and NR937. However, the edge stress is higher with NR compared to NR937, while in the central region, the stress is lower with NR than with NR937. This indicates that although the membrane deforms more with the structural sheet material (NR937), the stress distribution is more uniform across the membrane. This helps reduce potential fatigue loads and lowers the risk of material failure, improving the durability of the system.

4.3.3. *Power output*

The power output of the OWC WEC at different wave frequencies for both NR and NR937 materials is estimated based on the deformation of the flexible membrane and calculated using Eqs. (8)-(11). Additionally, a 1:20 scale ratio is applied to project the full-scale power output of the WEC system, as shown in Fig. 22. Compared to NR, the peak frequency of the WEC system's power output remains around 0.55 Hz when using NR937. However, the maximum power output increases significantly, with the output in the frequency range of 0.3 Hz to 0.6 Hz rising by approximately 3.2 to 3.9 times. According to Froude's similarity law, at

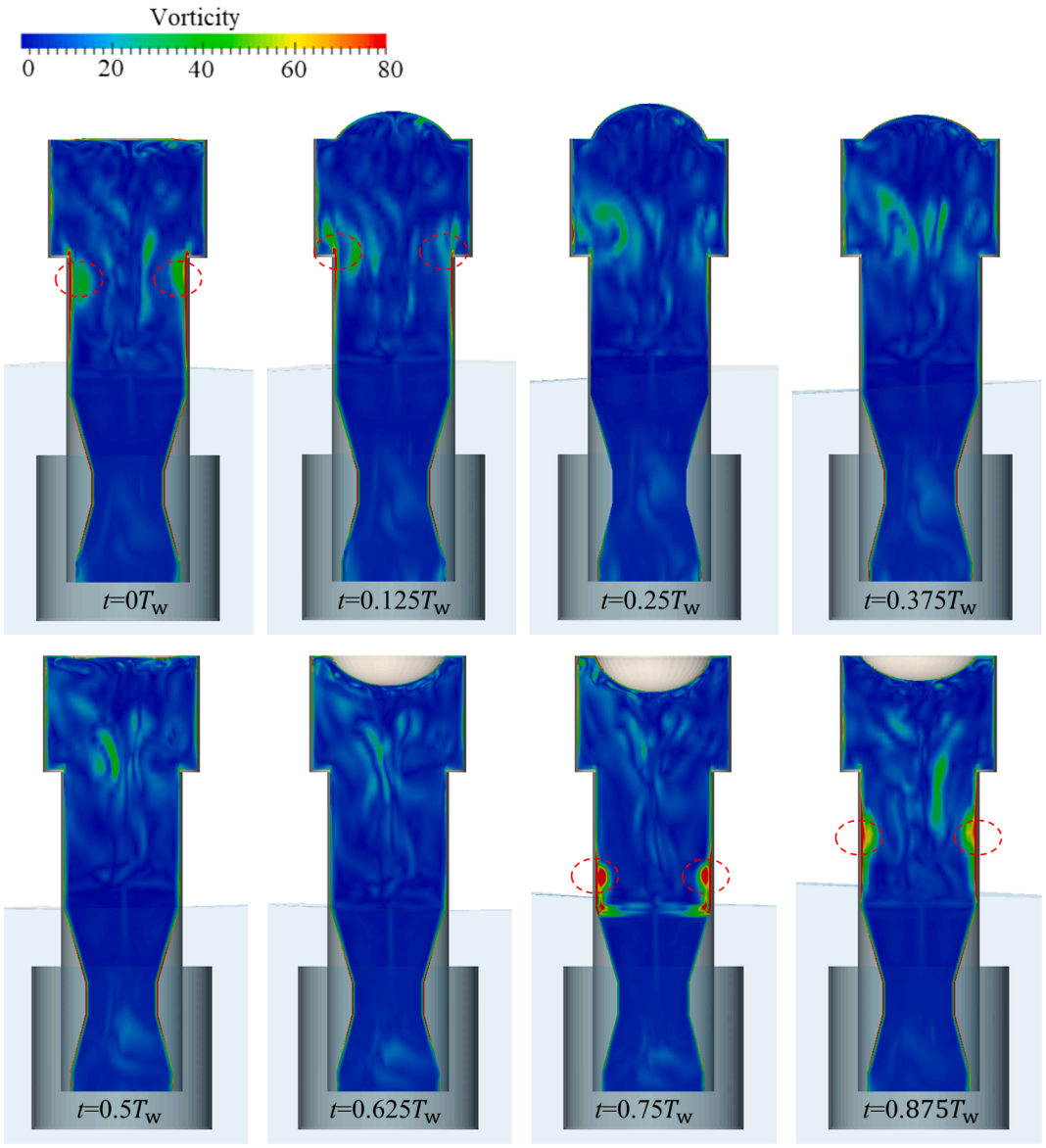

Fig. 12. Vorticity distribution in the air chamber at different instants within one wave period (LC1, $f_w = 0.55$ Hz).

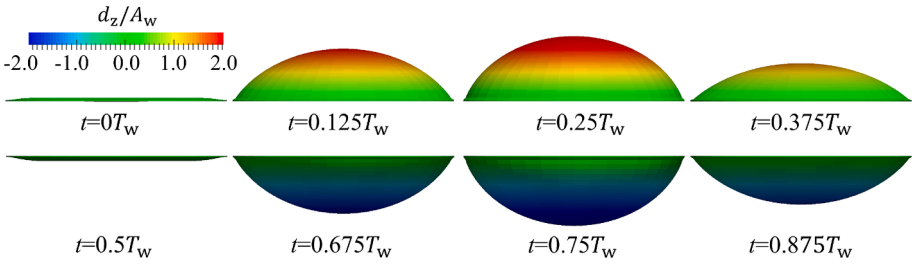

Fig. 13. Vertical deformation (d_z) of the membrane normalized by wave amplitude (A_w) at different instants during one wave period (LC1, $f_w = 0.55$ Hz).

full scale, the theoretical maximum power output of the WEC system increases from 135 kW to 445 kW when switching from NR to NR937, indicating a substantial improvement. This suggests that FlexWEC holds significant potential for future development.

4.4. Impact of pre-stretching on membrane

In flexible OWC WEC systems, pre-stretching is commonly applied to the flexible membrane to enhance power generation efficiency. This is because DEGs exhibit significantly improved charge storage capacity under pre-stretched conditions. Additionally, pre-stretching increases the membrane's stiffness, mitigating excessive deformation under external forces and enhancing mechanical stability. The resulting stiffness modification also shifts the system's natural frequency, allowing it to better align with the incident wave frequency and thereby improving wave energy capture efficiency.

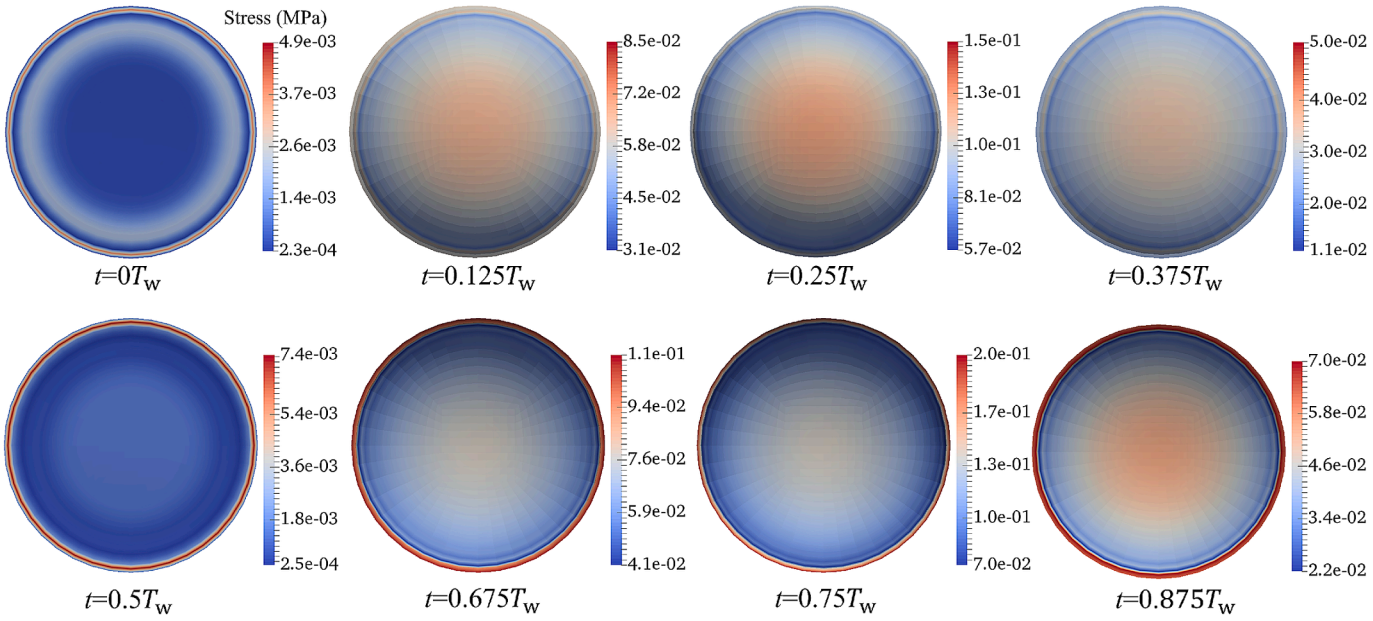

Fig. 14. Von Mises stress distribution on the surface of the membrane at different instants during one wave period (LC1, f_w = 0.55 Hz).

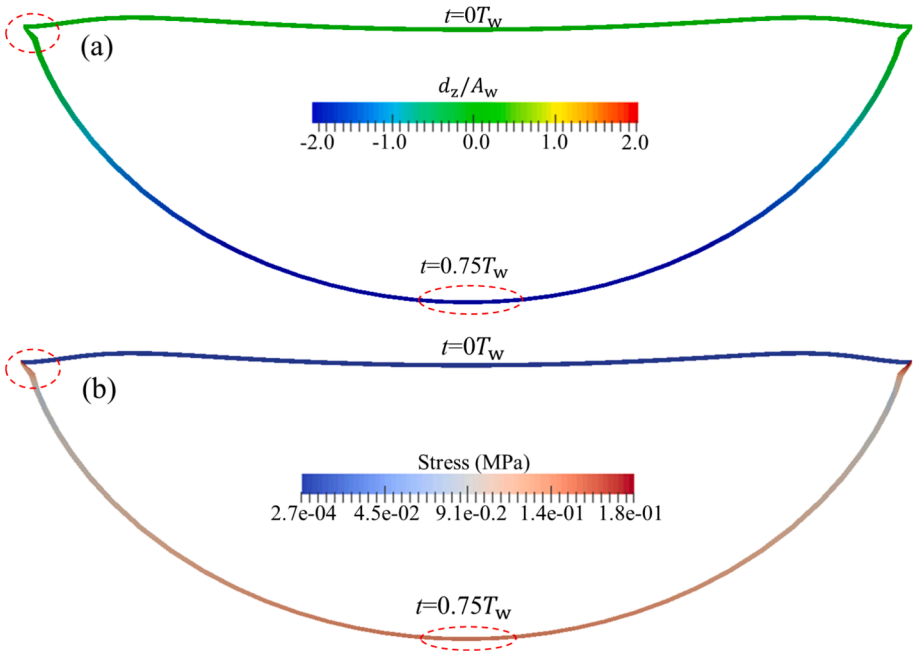

Fig. 15. Structural response of the membrane cross-section at two different instants (LC1, f_w = 0.55 Hz): (a) membrane's vertical deformation normalized by wave amplitude; (b) Von Mises stress.

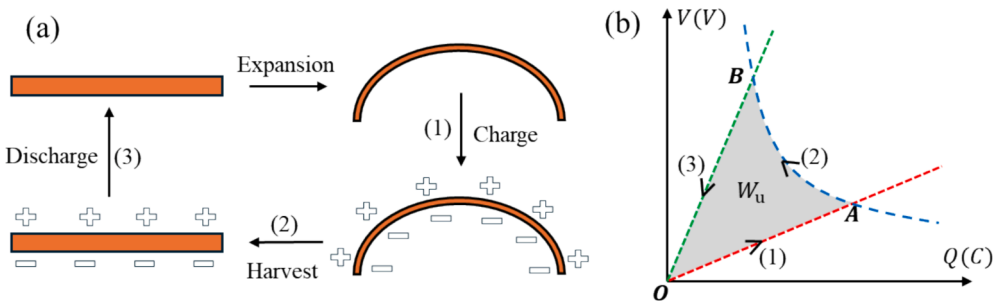

Fig. 16. Schematic diagram DEG membrane's energy generation: (a) membrane deformation; (b) Q-V plane.

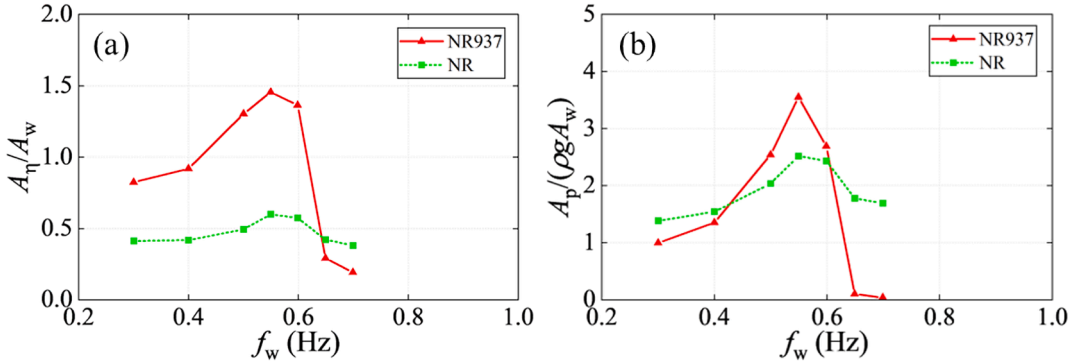

Fig. 17. Fluid dynamics under various wave frequencies (LC1 and LC2): (a) RAO of OWC in the collector; (b) pressure amplitude in the air-chamber.

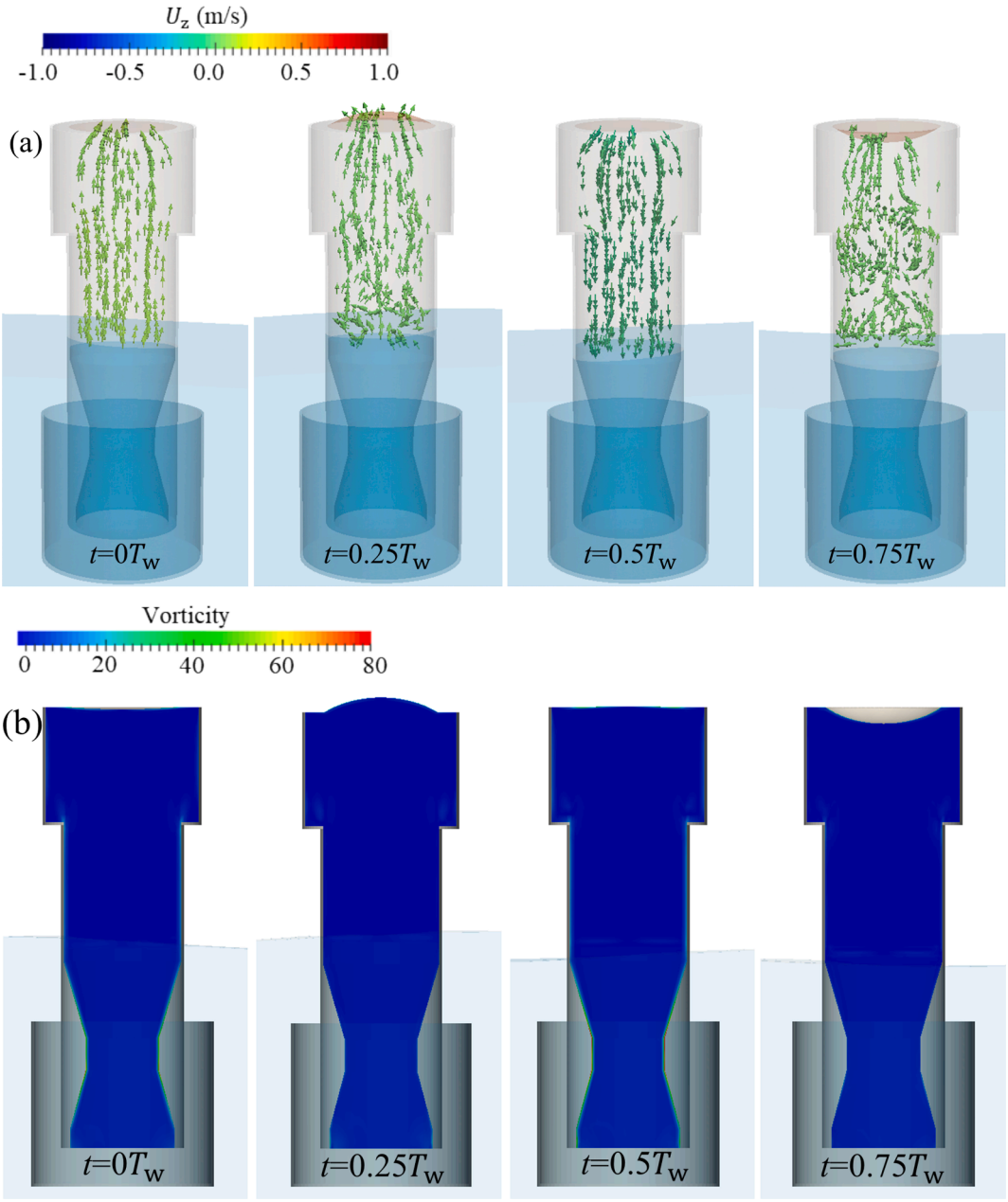

Fig. 18. Flow field in the air-chamber at different instants during one wave period (LC2, f_w = 0.55 Hz): (a) velocity field; (b) vorticity distribution.

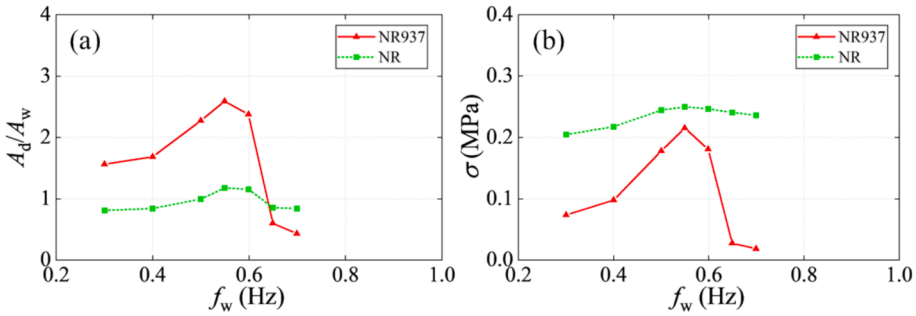

Fig. 19. Structural responses of the circular membrane with NR937 and NR at various wave frequencies (LC1 and LC2): (a) membrane centre deformation amplitude; (b) maximum Von Mises stress.

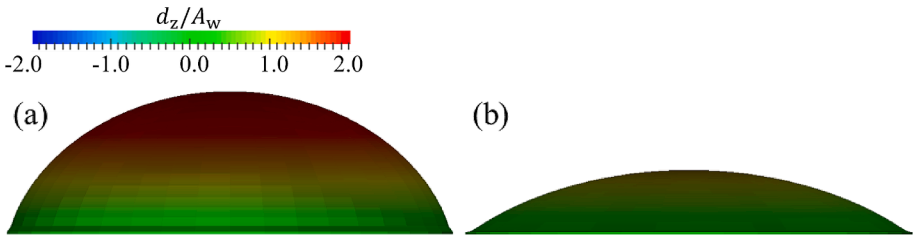

Fig. 20. Maximum deformation of the circular membrane at resonant frequencies (LC1 and LC2): (a) NR937 at $f_w = 0.55$ Hz; (b) NR at $f_w = 0.575$ Hz.

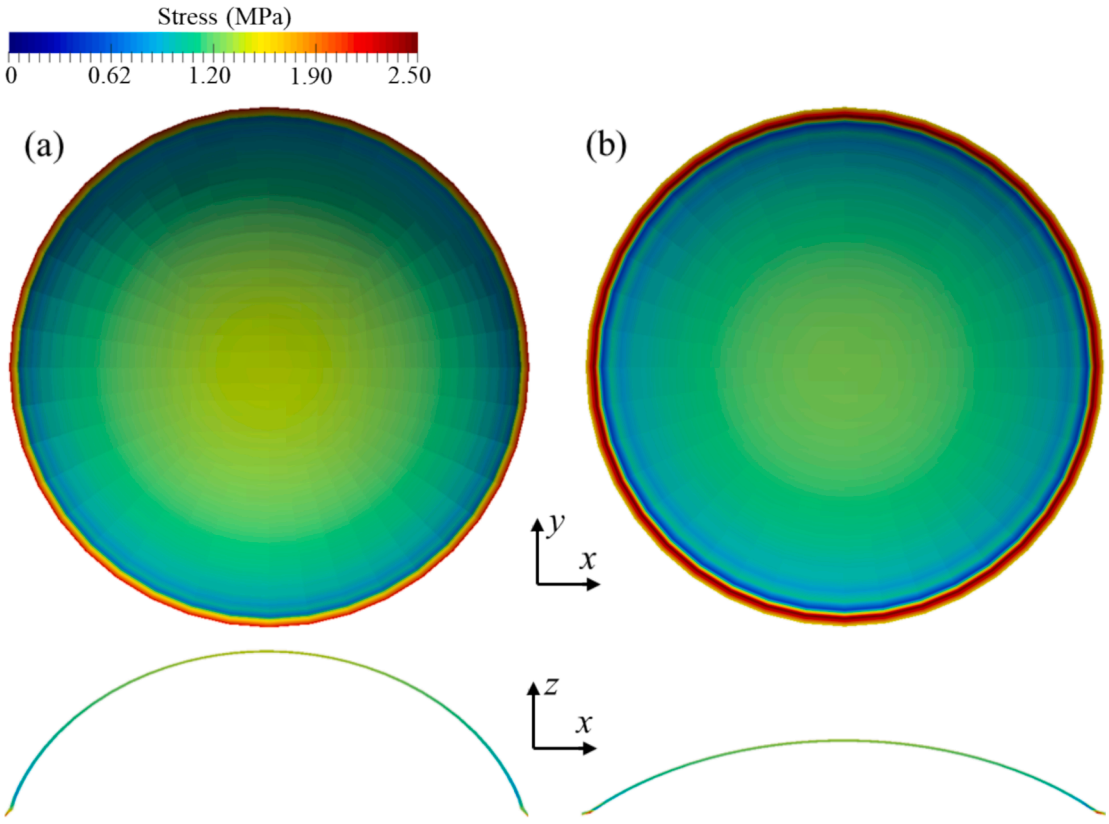

Fig. 21. Stress distribution on the circular membrane at the maximum deformation position (LC1 and LC2): (a) NR937; (b) NR.

In practical applications, pre-stretching can be implemented using either fixed mechanical frames or adaptive tensioning mechanisms. The most straightforward approach involves applying a predefined pre-stretch during installation by securing the membrane within a rigid structural frame or clamping system, ensuring consistent tension throughout operation. While this method is simple and widely adopted, it does not allow for real-time adjustments.

Alternatively, actively tunable pre-stretching systems could be integrated to dynamically adjust membrane tension in response to varying wave conditions. This could be achieved using pneumatic/hydraulic actuators or smart materials (such as shape-memory alloys or electro-active polymers) to regulate tension in real time. Such an approach

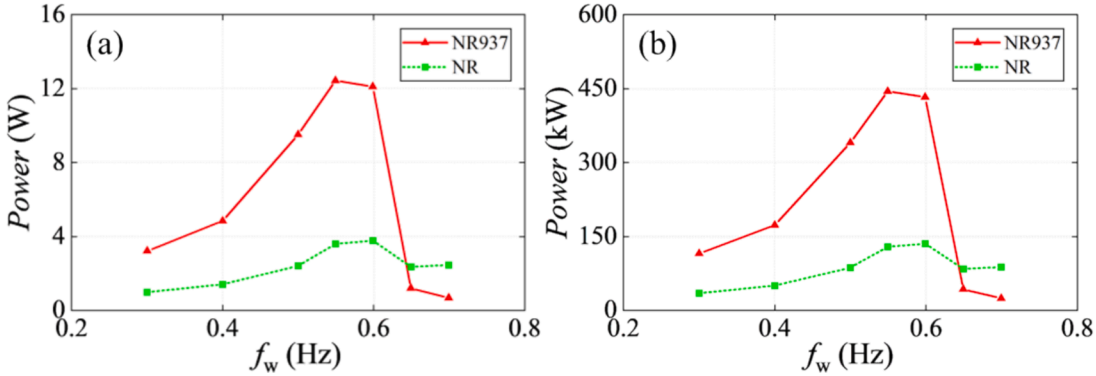

Fig. 22. Power estimation of the OWC WEC system (LC1 and LC2): (a) model scale; (2) full scale.

would enable the system to adapt to different sea states, optimizing resonance conditions and maximizing energy conversion efficiency. However, the practical implementation of tunable pre-stretching poses challenges due to increased structural complexity, energy consumption, and control requirements.

To assess the impact of pre-stretching on the performance of flexible OWC WEC systems, including fluid dynamics, structural responses, and power output, we conduct a comparative analysis of systems with and without a fixed pre-stretching.

4.4.1. Air-chamber pressure and OWC amplitude

Fig. 23 presents the RAO of the OWC (A_η/A_w) and the pressure variation amplitude (A_p) within the air chamber at different wave frequencies, considering a pre-stretching (λ_p) of 0.1 and without it. In both cases, A_η and A_p initially increase and then decrease as the wave frequency rises. However, the peak frequencies differ significantly between the two scenarios. When $\lambda_p = 0$, the peak frequency occurs at 0.55 Hz, while with $\lambda_p = 0.1$, the peak frequency shifts to 0.8 Hz. This shift is attributed to the increased stiffness of the flexible membrane due to pre-stretching, which raises the system's natural frequency. This finding suggests a potential method for dynamically tuning the resonance frequency of OWC WEC systems to better adapt to irregular wave conditions. Comparing the peak values of RAO and A_p under different pre-stretching conditions indicates that when the λ_p increases from 0 to 0.1, the peak A_p decreases by approximately 7 %, while the peak RAO decreases by about 41 %. This confirms the significant increase in system stiffness due to membrane pre-stretching.

The flow field within the air chamber, including velocity and vorticity fields under different pre-stretching conditions, is shown in Figs. 11, 12, and 24. Compared to the case with no pre-stretching, when $\lambda_p = 0.1$, the velocity differences across various regions of the air chamber at the same time are minimal, and the temporal variations are also reduced. Consequently, the vorticity magnitude decreases significantly, preventing the formation of distinct vortex structures. This indicates that the flow field within the air chamber becomes more stable when $\lambda_p = 0.1$.

4.4.2. Membrane deformation and stress distribution

To investigate the impact of pre-stretching on the structural dynamics of the flexible membrane, the deformation amplitude at the membrane centre and the maximum stress in the membrane at different wave frequencies are extracted and presented in Fig. 25. As λ_p increases from 0 to 0.1, the peak frequencies of membrane deformation and maximum stress shift significantly from 0.55 Hz to 0.8 Hz due to the increased stiffness of the WEC system. However, the peak values of membrane deformation and maximum stress show small variation. Compared to the case without pre-stretching, at $\lambda_p = 0.1$, the membrane deformation amplitude increases by approximately 9 %, while the maximum stress decreases by about 15 %.

The contour plots of maximum deformation and stress distribution for the flexible membrane under different pre-stretching conditions at the peak frequency are shown in Figs. 26 and 27. As λ_p increases from 0 to 0.1, the membrane's deformation shape deviates from a spherical cap. This is primarily due to the significant increase in stress at the membrane edges caused by pre-stretching, as shown in Fig. 27, which leads to a marked increase in out-of-plane stiffness in that region and a corresponding reduction in deformation amplitude. It is noteworthy that such a deformation pattern was not observed in the study by Moretti et al. [18], likely because they considered much larger deformation amplitudes. Additionally, Rosati et al.'s [13] reduced-order model assumes a spherical shape for the deformed membrane, a simplification that is clearly not applicable in the present case.

In addition, compared to the case with $\lambda_p = 0$, the flexible membrane experiences lower stress at both the edge and centre when $\lambda_p = 0.1$. However, due to pre-stretching, stress in other regions increases significantly, even though the vertical deformation amplitude in these areas remains relatively small. Overall, the stress distribution across the

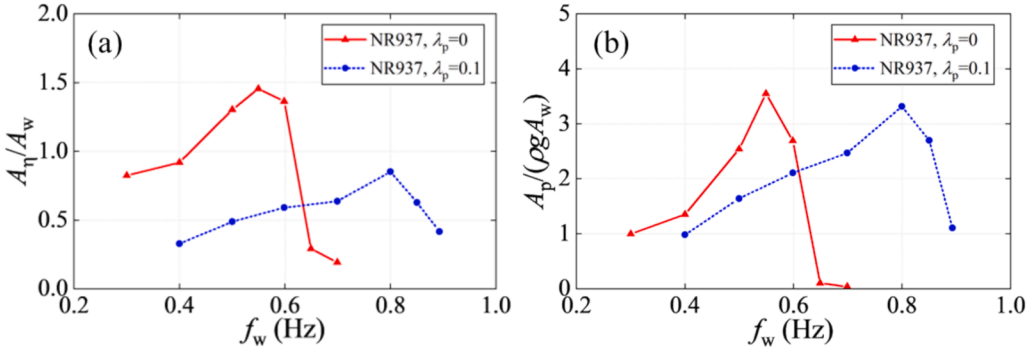

Fig. 23. Fluid dynamics under various wave frequencies (LC1 and LC3): (a) RAO of OWC in the collector; (b) pressure amplitude in the air-chamber.

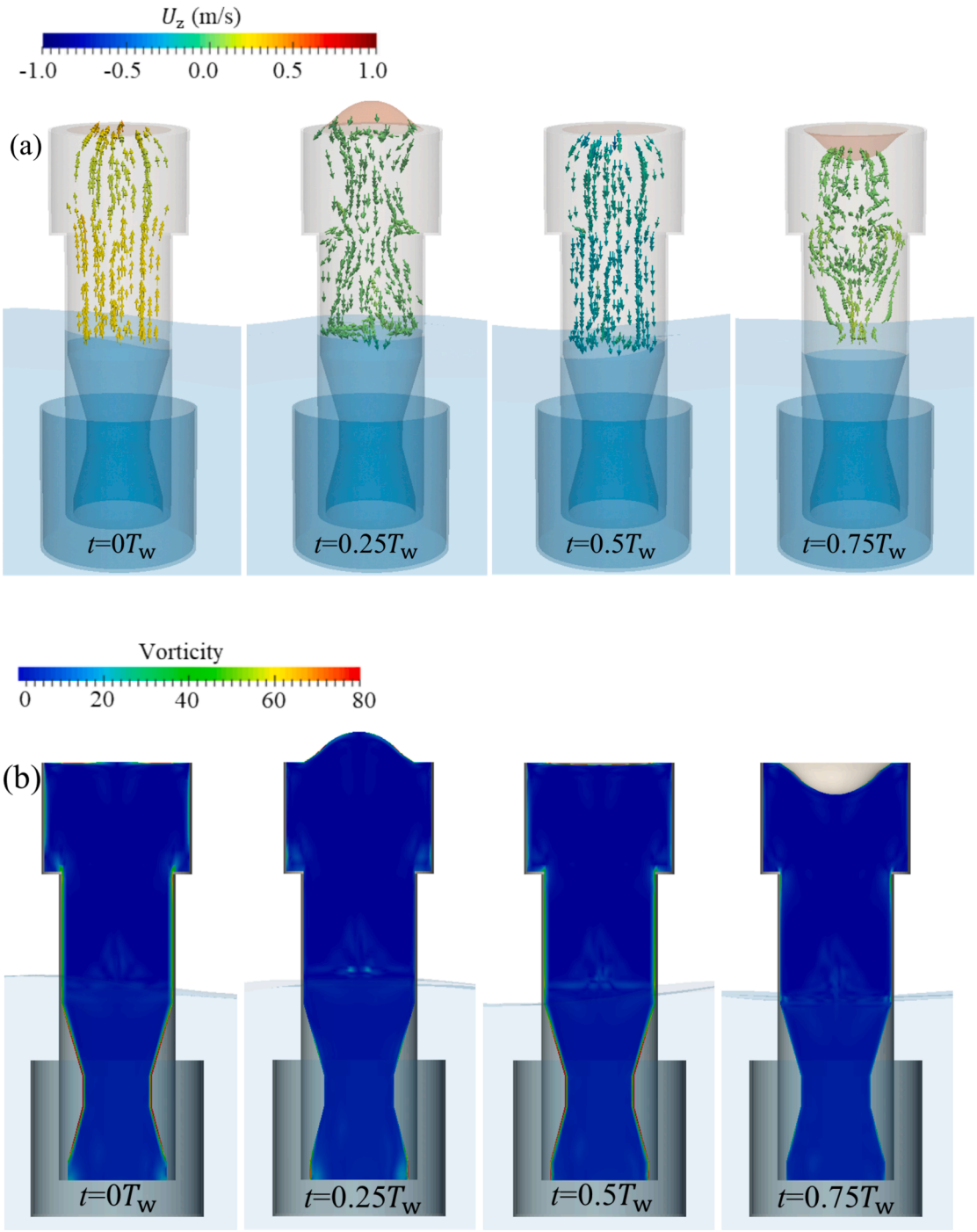

Fig. 24. Flow field in the air-chamber at different instants during one wave period (LC3, f_w = 0.8 Hz, λ_p = 0.1): (a) velocity field; (b) vorticity distribution.

membrane is more uniform at $\lambda_p = 0.1$, which is beneficial for reducing material fatigue loading.

4.4.3. Power output

The power output of the OWC WEC at different wave frequencies for $\lambda_p = 0$ and $\lambda_p = 0.1$ is calculated and shown in Fig. 28. Similar to the variation in the OWC's RAO with wave frequency, the peak power output occurs at $f_w = 0.55$ Hz for $\lambda_p = 0$ and at $f_w = 0.8$ Hz for $\lambda_p = 0.1$. As λ_p increases from 0 to 0.1, the maximum power output of the WEC system rises from 445 kW to 686 kW, an increase of approximately 54 %.

These results indicate that pre-stretching not only significantly alters the natural frequency of the WEC system but also enhances its power output, highlighting its potential as a dynamic tuning strategy for FlexWEC to better adapt to complex and variable sea conditions.

Additionally, it is important to note that the current method for estimating the OWC WEC system's power output, as defined by Eq. (8), assumes that the deformed membrane adopts a spherical shape. However, as illustrated in Fig. 26, when $\lambda_p = 0.1$, the membrane no longer approximates a spherical shape, implying that the estimated power output is an approximation rather than an exact value. To accurately determine the electrical power generated by the DEG PTO system, a fully coupled fluid–structure-electricity model is required.

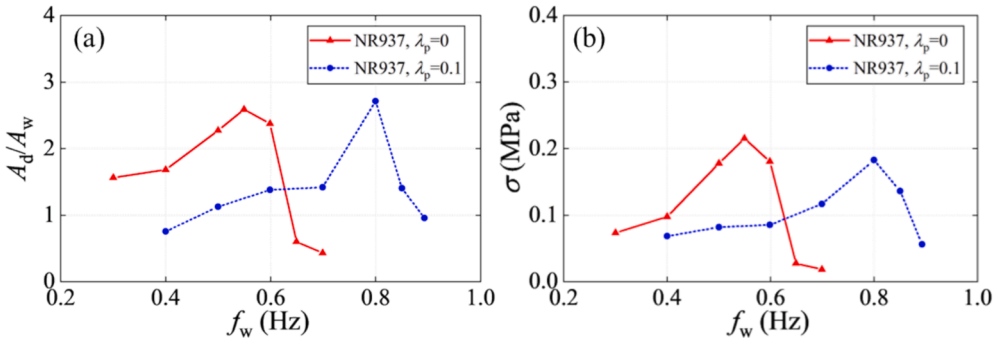

Fig. 25. Structural responses of the circular membrane with and without pre-stretching under various wave frequencies (LC1 and LC3): (a) membrane centre deformation amplitude; (b) maximum Von Mises stress.

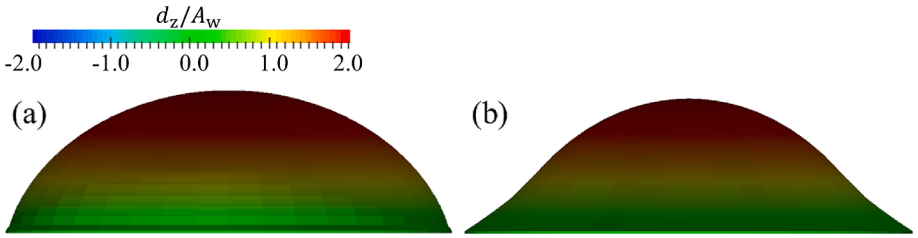

Fig. 26. Maximum deformation of the circular membrane at resonant frequencies (LC1 and LC3): (a) NR937 with $\lambda_p = 0$ at $f_w = 0.55$ Hz; (b) NR937 with $\lambda_p = 0.1$ at $f_w = 0.65$ Hz.

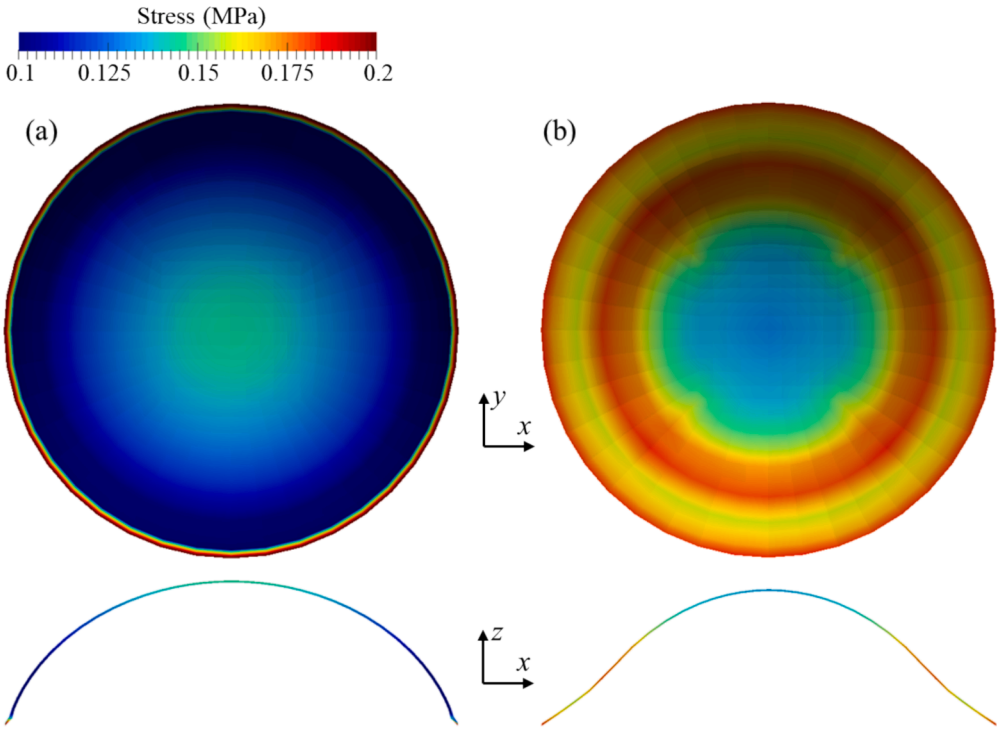

Fig. 27. Stress distribution on the circular membrane at the maximum deformation position (LC1 and LC3): (a) NR937 with $\lambda_p = 0$; (b) NR937 with $\lambda_p = 0.1$.

5. Conclusions

In this study, a structural sheet material with pattern 937 is developed for application in the flexible OWC WEC. Uniaxial tests are conducted to characterize the material's behaviour, and the hyper-elastic YEOH model is employed to describe its nonlinear response. The YEOH model constants are derived by fitting the stress–strain curves from experimental data. Furthermore, using a high-fidelity FSI tool, the response of a flexible OWC WEC model utilizing the structural sheet material is simulated and compared with the performance of the system using conventional flexible material, natural rubber. The effects of membrane pre-stretching on the FlexWEC's performance are also investigated. The analysis focused on the flow field within the air chamber, the structural response of the flexible membrane, and the

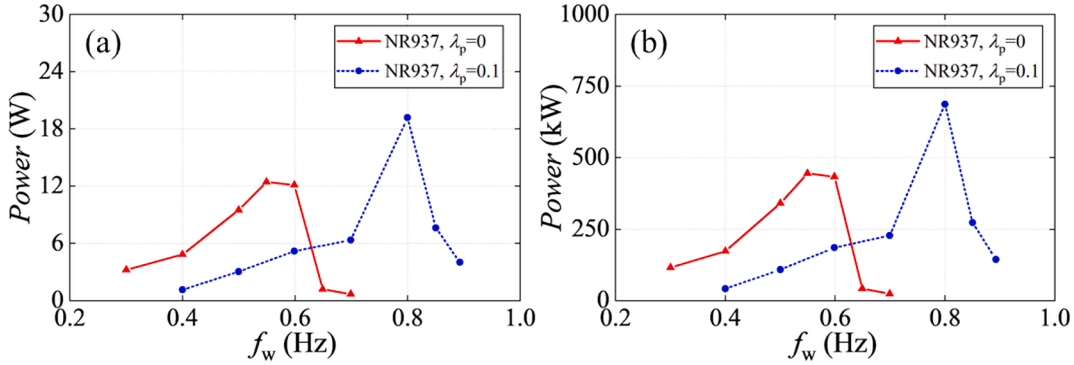

Fig. 28. Power estimation of the OWC WEC system (LC1 and LC3): (a) model scale; (2) full scale.

power output of the OWC system, leading to several key conclusions from the numerical results.

Compared to natural rubber (NR), the perforated design of the structural sheet material (NR937) significantly reduces material usage and overall weight, leading to cost savings and facilitating the scaling up of FlexWEC systems. Additionally, the structural sheet material exhibits much lower stiffness, particularly at lower strain levels. This reduction in stiffness has minimal impact on the natural frequency of the WEC system. At resonance, the membrane deformation amplitude increases by approximately 143 % when using the structural sheet material, while the air chamber pressure amplitude only increases by about 40 %. This indicates that the structural sheet material enables greater membrane deformation under relatively lower pressure, resulting in a 245 % increase in the WEC system's power output. Moreover, despite the increased deformation, the maximum membrane stress at resonance decreases by about 14 %, and the stress distribution becomes more uniform across the membrane, indicating reduced fatigue loading and a lower risk of material failure. On the other hand, a small membrane pre-stretching of 10 % increases the natural frequency of the WEC system from 0.55 Hz to 0.8 Hz. While the air chamber pressure amplitude decreases by about 7 %, the membrane deformation amplitude increases by approximately 9 %, leading to a 54 % increase in power output. Additionally, pre-stretching reduces the maximum membrane stress by about 15 % and results in a more uniform stress distribution, although the deformed membrane shape is no longer approximately spherical. Pre-stretching offers a potential strategy for dynamically tuning FlexWEC to better capture energy under complex and variable sea conditions.

The present work is significant for enhancing the power output of FlexWECs and optimizing the structural response of the flexible membrane. Additionally, it offers new insights into the dynamic control of FlexWEC systems to better adapt to marine environments. However, the current numerical simulations do not account for the DEG PTO, thus neglecting the influence of the electric field on the structural response of the flexible membrane. Although a reduced model is used to estimate the power output of the WEC system, this approach has certain limitations. Therefore, future work will focus on conducting fluid–structure-electric coupling simulations for FlexWEC to further improve the understanding of its complex responses and power output performance.

CRediT authorship contribution statement

Yang Huang: Writing – review & editing, Writing – original draft, Visualization, Validation, Software, Methodology, Investigation, Formal analysis, Data curation, Conceptualization. **Guillermo Idarraga:** Writing – review & editing, Visualization, Methodology, Investigation, Formal analysis, Data curation, Conceptualization. **Farhad Abad:** Writing – review & editing, Software, Formal analysis, Data curation, Conceptualization. **Qing Xiao:** Writing – review & editing, Validation, Supervision, Software, Resources, Project administration, Methodology, Investigation, Funding acquisition, Formal analysis, Conceptualization. **Liu Yang:** Supervision, Resources, Methodology, Funding acquisition, Formal analysis, Conceptualization. **Saishuai Dai:** Validation, Resources, Investigation, Formal analysis, Data curation. **Saeid Lotfian:** Writing – review & editing, Visualization, Validation, Formal analysis. **Feargal Brennan:** Supervision, Resources, Funding acquisition.

Declaration of competing interest

The authors declare that they have no known competing financial interests or personal relationships that could have appeared to influence the work reported in this paper.

Acknowledgements

This research was supported by an Engineering and Physical Sciences Research Council (EPSRC) Grant "Bionic Adaptive Stretchable Materials for WEC (BASM-WEC)" (EP/V040553/1).

Data availability

Data will be made available on request.

References

[1] Babarit A. Ocean wave energy conversion: resource, technologies and performance [M]. Elsevier; 2017.
[2] Falcão AFO. Wave energy utilization: A review of the technologies[J]. Renew Sustain Energy Rev 2010;14(3):899–918.
[3] Collins I, Hossain M, Dettmer W, et al. Flexible membrane structures for wave energy harvesting: A review of the developments, materials and computational modelling approaches[J]. Renew Sustain Energy Rev 2021;151:111478.
[4] Vertechy R, Fontana M, Papini GPR, et al. In-tank tests of a dielectric elastomer generator for wave energy harvesting[C]//Electroactive Polymer Actuators and Devices (EAPAD) 2014. SPIE 2014;9056:332–42.
[5] Pecher A, Kofoed JP. Handbook of ocean wave energy[M]. Springer. Nature 2017.
[6] Kornbluh RD, Pelrine R, Prahlad H, et al. From boots to buoys: promises and challenges of dielectric elastomer energy harvesting[J]. Electroactivity in polymeric materials 2012:67–93.
[7] Jean P, Wattez A, Ardoise G, et al. Standing wave tube electro active polymer wave energy converter[C]//Electroactive Polymer Actuators and Devices (EAPAD) 2012. SPIE 2012;8340:75–95.
[8] Kaltseis R, Keplinger C, Koh SJA, et al. Natural rubber for sustainable high-power electrical energy generation[J]. RSC Adv 2014;4(53):27905–13.
[9] Liu Z, Zhang R, Xiao H, et al. Survey of the mechanisms of power take-off (PTO) devices of wave energy converters[J]. Acta Mech Sin 2020;36:644–58.
[10] Suo Z. Theory of dielectric elastomers[J]. Acta Mech Solida Sin 2010;23(6):549–78.
[11] Pelrine R, Kornbluh RD, Eckerle J, et al. Dielectric elastomers: generator mode fundamentals and applications[C]//Smart Structures and Materials 2001: Electroactive Polymer Actuators and Devices. SPIE 2001;4329:148–56.
[12] Vertechy R, Fontana M, Papini GPR, et al. Oscillating-water-column wave-energy-converter based on dielectric elastomer generator[C]//Electroactive Polymer Actuators and Devices (EAPAD) 2013. SPIE 2013;8687:130–42.
[13] Rosati Papini GP, Vertechy R, Fontana M. Dynamic model of dielectric elastomer diaphragm generators for oscillating water column wave energy converters[C]//

Smart Materials, Adaptive Structures and Intelligent Systems. Am Soc Mech Eng 2013;56031:V001T03A038.
[14] Falcão AFO, Henriques JCC. Oscillating-water-column wave energy converters and air turbines: A review[J]. Renew Energy 2016;85:1391–424.
[15] Moretti G, Rosati G P P, Alves M, et al. Analysis and design of an oscillating water column wave energy converter with dielectric elastomer power take-off[C]// International Conference on Offshore Mechanics and Arctic Engineering. American Society of Mechanical Engineers, 2015, 56574: V009T09A023.
[16] Moretti G, Papini GPR, Righi M, et al. Resonant wave energy harvester based on dielectric elastomer generator[J]. Smart Mater Struct 2018;27(3):035015.
[17] Rosati Papini GP, Moretti G, Vertechy R, et al. Control of an oscillating water column wave energy converter based on dielectric elastomer generator[J]. Nonlinear Dyn 2018;92:181–202.
[18] Moretti G, Rosati Papini GP, Daniele L, et al. Modelling and testing of a wave energy converter based on dielectric elastomer generators[J]. Proceedings of the Royal Society A 2019;475(2222):20180566.
[19] Moretti G, Malara G, Scialò A, et al. Modelling and field testing of a breakwater-integrated U-OWC wave energy converter with dielectric elastomer generator[J]. Renew Energy 2020;146:628–42.
[20] Abad F, Lotfian S, Dai S, et al. Experimental and computational analysis of elastomer membranes used in oscillating water column WECs[J]. Renew Energy 2024;226:120422.
[21] Righi M, Moretti G, Forehand D, et al. A broadbanded pressure differential wave energy converter based on dielectric elastomer generators[J]. Nonlinear Dyn 2021; 105(4):2861–76.
[22] Schumacher C, Marschner S, Gross M, et al. Mechanical characterization of structured sheet materials[J]. ACM Transactions on Graphics (TOG) 2018;37(4): 1–15.
[23] Ellenbroek WG, Zeravcic Z, van Saarloos W, et al. Non-affine response: Jammed packings vs. spring networks[J]. Europhys Lett 2009;87(3):34004.
[24] O'Rourke J. How to fold it: the mathematics of linkages, origami, and polyhedra [M]. Cambridge University Press; 2011.
[25] Ellenbroek WG, Hagh VF, Kumar A, et al. Rigidity loss in disordered systems: Three scenarios[J]. Phys Rev Lett 2015;114(13):135501.
[26] Huang Y, Xiao Q, Idarraga G, et al. Novel computational fluid dynamics-finite element analysis solution for the study of flexible material wave energy converters [J]. Phys Fluids 2023;35(8).
[27] Coruba (2024). https://www.coruba.co.uk/, accessed 20th October 2023.
[28] Idarraga G, Yang L, Abad F, et al. Hyperelastic modelling of elastomers for wave energy convertors[C]//International Conference on Offshore Mechanics and Arctic Engineering. American Society of Mechanical Engineers, 2023, 86854: V003T03A001.
[29] Idarraga G, Yang L, Abad F, et al. Hyperelastic behaviour of elastomers for wave energy applications [J]. Ocean Eng 2024. second review.
[30] Yeoh OH. Some forms of the strain energy function for rubber[J]. Rubber Chem Technol 1993;66(5):754–71.
[31] Huang Y, Xiao Q, Idarraga G, et al. Numerical Analysis of Flexible Tube Wave Energy Convertor Using CFD-FEA Method[C]//International Conference on Offshore Mechanics and Arctic Engineering. American Society of Mechanical Engineers, 2023, 86908: V008T09A062.
[32] Huang Y, Xiao Q, Alarcon G I, et al. A CFD-FEM analysis for Anaconda WEC with mooring lines[C]//Proceedings of the 15th European Wave and Tidal Energy Conference 2023. 2023: 163.
[33] Huang Y, Idarraga G, Xiao Q, et al. Numerical analysis of structured sheet material in flexible oscillating water column wave energy converter[C]//43rd International Conference on Ocean, Offshore & Arctic Engineering. 2024: OMAE2024-121318.
[34] Berberović E, van Hinsberg NP, Jakirlić S, et al. Drop impact onto a liquid layer of finite thickness: Dynamics of the cavity evolution[J]. Physical Review E—Statistical, Nonlinear, and Soft Matter. Physics 2009;79(3):036306.
[35] Jasak H. Error analysis and estimation in the Finite Volume method with applications to fluid flows[J]. 1996.
[36] Jasak H, Jemcov A, Tukovic Z. OpenFOAM: A C++ library for complex physics simulations[C]//International workshop on coupled methods in numerical dynamics. 2007, 1000: 1-20.
[37] Dhondt G. Calculix crunchix user's manual version 2.12[J]. Munich, Germany, accessed Sept, 2017, 21: 2017.
[38] Bungartz HJ, Lindner F, Gatzhammer B, et al. preCICE–a fully parallel library for multi-physics surface coupling[J]. Comput Fluids 2016;141:250–8.
[39] Degroote J, Bathe KJ, Vierendeels J. Performance of a new partitioned procedure versus a monolithic procedure in fluid–structure interaction[J]. Comput Struct 2009;87(11–12):793–801.
[40] Lindner F, Mehl M, Uekermann B. Radial basis function interpolation for black-box multi-physics simulations[J]. 2017.
[41] Higuera P, Lara JL, Losada IJ. Three-dimensional interaction of waves and porous coastal structures using OpenFOAM®. Part I: Formulation and validation[J]. Coast Eng 2014;83:243–58.
[42] Higuera P, Lara JL, Losada IJ. Three-dimensional interaction of waves and porous coastal structures using OpenFOAM®. Part II: Application[J]. Coast Eng 2014;83: 259–70.
[43] Dhondt G. Calculix crunchix user's manual version 2.12[J]. Munich, Germany, accessed Sept, 2017, 21: 2017.
[44] Vertechy R, Papini Rosati GP, Fontana M. Reduced model and application of inflating circular diaphragm dielectric elastomer generators for wave energy harvesting[J]. J Vib Acoust 2015;137(1):011004.